Results in Engineering 31 (2026) 111488

Contents lists available at ScienceDirect

Results in Engineering

journal homepage: www.sciencedirect.com/journal/results-in-engineering

Research paper

# Mechanical performance, energy dissipation, and failure mode evolution of $CO_2$ mineralized cement paste backfill incorporating mine tailings

Zahid Hussain [a,b,c], Jianxin Fu [a,b,*], Song Weidong [a,b], Jiajie Li [a,b], Erol Yilmaz [d]

[a] School of Resources and Safety Engineering, University of Science and Technology Beijing, Beijing 100083, China
[b] Key Laboratory of High-Efficient Mining and Safety of Metal Mines, Ministry of Education, University of Science and Technology Beijing, Beijing 100083, China
[c] Mining Engineering Department, Karakoram International University, KIU, Gilgit 15,100 Pakistan
[d] Department of Civil Engineering, Recep Tayyip Erdogan University, Fener, Rize, Turkey

ARTICLE INFO

*Keywords:*
Mineral carbonation
Cement paste backfill (CPB)
Mine tailings
Carbon sequestration
Failure modes
Energy dissipation

ABSTRACT

Mining industry generates ~13 billion tons of tailings annually while contributing nearly 10% of global emissions, demanding integrated strategies for waste management. Mineralized cemented paste backfill (CPB) offers dual-function solution for structural ground support and in-situ carbon sequestration; however, effects of $CO_2$ injection on failure mechanics, energy dissipation, microstructural evolution, and carbon sequestration efficiency remain insufficiently understood. This study establishes the kinetic carbonation window for mineralized tailing-based cement paste backfill (MTCPB) by investigating $CO_2$ injection duration (0-20 min) and curing age (3, 7, 14 days) on mechanical performance, failure mode evolution, energy dissipation, and carbon sequestration capacity using uniaxial compressive strength (UCS), scanning electron microscopy with energy dispersive spectroscopy (SEM-EDS), thermogravimetric analysis with differential scanning calorimetry (TGA-DSC), and Fourier-transform infrared spectroscopy (FTIR). An optimal 10-min $CO_2$ injection duration under these specific conditions elevated UCS from 2.10 to 2.54 MPa, energy absorption from 3.53 to 5.47 MJ/m$^3$ (54.9%), transforming failure mode from shear-dominated to tensile splitting, a structural safety outcome of greater significance than peak strength alone. Portlandite content decreased from 2.45% (control) to 1.18% (optimal), confirming substantial $Ca(OH)_2$ consumption, while carbonate content increased from 4.64% to 5.25%, with peak $CO_2$ uptake of 6.32%. Beyond optimal window, overcarbonation triggered surface passivation and matrix heterogeneity, reducing elastic modulus by 55% without measurable mineralogical benefit. FTIR confirmed $Ca(OH)_2$ depletion and $CO_2$-driven ettringite-to-gypsum transformation. These findings advance backfill design toward performance-based paradigm integrating failure-mode control, microstructural optimization, and sustainable co-disposal of mine tailings and waste $CO_2$, offering scalable, evidence-based foundation for carbon-negative underground backfilling.

## 1. Introduction

As one of the oldest human activities, the mining industry has made indelible contributions to social development and modern industrialization [1,2]. With the growing demand for minerals and the depletion of shallow resources, mining activities have been raised and shifted to deep underground mining [2] . This transition generates two parallel and interconnected waste streams, mine tailings and carbon emissions that demand integrated rather than sequential solutions in the field [3,4]. Globally, mine sector generates 13 billion tons of mine tailings annually [5,6], stored in surface tailings dams that pose persistent risks of heavy metal leaching and catastrophic dam failure [7–9] . The mining industry accounts for approximately 10% of global energy-related greenhouse gas emissions, with major companies such as Rio Tinto emitting 584.6 million tons of $CO_2$ equivalent annually, while Vale and BHP produce 505.2 and 418.7 million tons, respectively [10,11]. In 2020, the global emission of $CO_2$ was 36 billion tons, with its concentration in the atmosphere increased to 400 ppm from the pre-industrial 280 ppm [12–14]. Under the current trajectory, 56 gigatons of $CO_2$ will accumulate by 2030, far exceeding the 25 billion tons capture threshold required for climate stability [15,16]. The convergence of these two challenges that are unmanaged tailings disposal and unabated $CO_2$ emissions create an unprecedented opportunity to use mine tailings and a reactive medium for permanent $CO_2$ mineralization, simultaneously

* Corresponding author at: School of Resources and Safety Engineering, University of Science and Technology Beijing, Beijing 100083, China.
*E-mail address:* fujun0011@126.com (J. Fu).

https://doi.org/10.1016/j.rineng.2026.111488
Received 21 April 2026; Received in revised form 28 May 2026; Accepted 9 June 2026
Available online 12 June 2026
2590-1230/© 2026 Published by Elsevier B.V. This is an open access article under the CC BY-NC-ND license (http://creativecommons.org/licenses/by-nc-nd/4.0/).

eliminating two waste streams through a single engineered process of mineralized backfill.

The underground cement paste backfill (CPB) represents the most technically and economically mature platform for realizing the dual waste co-disposal objective. CPB simultaneously provides structural ground support to prevent subsidence, enabling complete ore recovery, and serves as a repository for processed mine tailings [17]. In practice, CPB must achieve a uniaxial compressive strength (UCS) of at least 0.7 MPa for self-supporting stopes and 1.0 MPa for stopes adjacent to active mining zones, with long-term stability requiring $\geq$1.0 MPa beyond 91 days [18,19]. The mechanical performance of CPB is governed by a complex interplay of binder content, water-to-cement ratio, tailings particles size distribution [20], curing conditions [21,22], and time-dependent hydration product evolution [23,24,198]. Ghirian and Fall demonstrated that ongoing suction development and cement hydration drive significant UCS improvement with time in insulated-undrained high column testing [25]. Kesimal et al. showed binder mixture optimization is critical for sulphide-rich tailings CPB strength [26], while Cao et al. concluded that the mechanical properties of tailing-based CPBs are tied greatly to the inner microstructure of tailings [19]. Zhang et al. reported that particle size distribution (PSD) governs the workability of tailing-based filling materials [27,28]. Collectively, these studies establish that CPB performance is highly system-specific and cannot be generalized without characterizing the full microstructural and compositional response of the specific tailings-binder system under study.

Mineral carbonation (MC), the accelerated reaction of $CO_2$ with calcium- and magnesium-bearing minerals to stable carbonate phases, has emerged as the most thermodynamically reliable pathway within the realm of carbon capture, utilization, and storage (CCUS) technology [29–33]. Many researchers have already used methods for co-disposing mine tailings and waste $CO_2$ in the filling of goaf in the form of mineralized backfill [34–40]. The primary carbonation methods applied to cementitious systems include carbon curing of hardened specimens, dry carbonation of aggregates, and wet slurry carbonation during mixing, with the latter being most compatible with CPB preparation workflows [41–43]. The main cement constituents, $C_2S$ and $C_3S$ react with $CO_2$ to form carbonated products responsible for early strength enhancement. Studies have shown that carbonation significantly reduces porosity and increases microstructural compactness through $CaCO_3$ precipitation and pore refinement [34,35]. Cement ratios and wastes affect carbon sequestration [36,37]. $CO_2$ integration can increase the UCS of mineralized backfill due to the formation of carbonated and hydrated products, which cause porosity reduction, pore refinement, and densification of the micro-structure [35]. These collective findings establish that mineralized CPB has the theoretical basis to simultaneously exceed mechanical performance targets and deliver measurable carbon sequestration, making MC a candidate material for backfill fill systems integrated with $CO_2$ demanded by modern sustainable mining practices.

Research on carbonated CPB has progressed substantially over the past decade, establishing several important but partial insights. Studies have confirmed that $CO_2$ integration increases the UCS of mineralized backfill through the formation of carbonated and hydrated products that cause porosity reduction and microstructural densification [35,36]. Incorporating mineral carbonation with cement-based CPB has been shown to improve strength, toughness, and ductility relative to conventional hydration-only systems [38,39]. Research on the carbonation of OPC-based building materials has established that $Ca(OH)_2$ is the primary reactive precursor, with C-S-H decalcification as a secondary carbonation pathway [40,10]. Low-field nuclear magnetic resonance (LF-NMR) has been successfully applied to characterize pore size evolution in cementitious materials [44–46], and SEM-EDS has been used to map elemental distribution in hydrated matrices [47–50]. TGA has been employed to quantify Portlandite content and to estimate carbonation degree in cured specimens [51–53]. These contributions collectively demonstrate the technical feasibility of mineral carbonation in the CPB context. However, the existing body of literature is characterized by four critical limitations that constrain its translational value for the field-scale application of mineralized backfill design.

First, previous studies have largely evaluated carbonation effects on UCS as a single scalar output without characterizing how carbonation intensity reshapes the complete stress-strain response, failure mode transition, or post-peak fracture behavior, which are the parameters that actually govern structural safety in dynamic underground environments. Second, the relationship between $CO_2$ injection rate and the energy dissipation capacity of CPB has not been established. Third, while microstructural studies have reported qualitative SEM observations of carbonation products, no study has established a quantitative stoichiometric threshold that demarcates the transition from beneficial carbonation to detrimental surface passivation in mineralized CPB systems. Fourth, systematic multi-technique characterization integrating mechanical testing, SEM-EDS stoichiometry, FTIR bond characterization, failure modes evaluation, energy-dissipation analysis, and TGA-DSC carbon quantification across the full spectrum of $CO_2$ injection rates has not been conducted for mineralized CPB, leaving the carbonation mechanism, its kinetic limits, and its sequestration efficiency unresolved as an integral system. As a consequence, current practices rely on empirical trial-and-error injection protocols rather than science-based design specifications. This is a critical barrier to the safe, reproducible, and environmentally accountable field application of carbonated backfill systems.

To address these interconnected gaps, this study presents a systematic, multi-scale investigation of the effects of $CO_2$ injection duration and curing age on the mechanical performance, failure mode evolution, energy dissipation, elastic stiffness, microstructural-stoichiometric transformation, and carbon sequestration efficiency of mineralized tailing-based cement paste backfill (MTCPB) prepared through direct $CO_2$ injection into paste slurry during stirring in a multi-functional closed reactor. Specifically, this study: (i) establishes a six-stage stress-strain failure framework for MTCPB across the full carbonation spectrum, including failure mode as a controllable engineering design output; (ii) quantifies the energy dissipation behavior of carbonated CPB through total, elastic, and dissipated strain energy analysis, providing a toughness-based design criterion that complements UCS; (iii) develops curing-age-specific predictive models for UCS and elastic modulus as a function of $CO_2$ injection duration; (iv) establishes a quantitative stoichiometric passivation threshold through systematic SEM-EDS atomic ratio analysis, providing a field applicable process control marker; and (v) delivers an integrated multi-technique chemical characterization combining FTIR bond analysis and TGA-DSC carbon accounting that fully resolves the dual pathway carbonation mechanism and its kinetic limits. While prior work on mineralized paste backfill has established the general benefits of $CO_2$ mineralization for CPB, these contributions of the present study collectively advance the CPB design from a strength-only criterion toward a performance-based paradigm, establishing the scientific foundation for mineralized underground backfilling as a scalable and evidence-based practice.

## 2. Materials and methods

### 2.1. Materials

- Tailings and binder

White Portland cement was utilized in this experiment due to the fact that the paramagnetic behavior of ordinary Portland cement (OPC) affects the results of nuclear magnetic resonance (NMR) to some degree. It was sourced from the production facility in Weifang, China. The particle size distribution was measured with a laser particle size analyzer (Malvern Mastersizer 2000) that was capable of measuring particles from the 0.01 μm to 2 mm range. For the preparation of cement paste backfill, the tailings should have a minimum of 15% of the total volume

of particles smaller than 20 micrometers [54]. The PSD data shows that this fraction is attributed to 35% of tailings meeting the required criteria of filling materials. Table 1. shows fundamental physical characteristics like coefficient of uniformity (Cu), coefficient of curvature (Cc), specific gravity (Sg), specific surface area (SS), and bulk density (ρ) having values of 11.46 μm, 0.61 μm, 1.47, 1022.74 $m^2$/kg, 1.12 g/$cm^3$, respectively. The established mean particle diameter ($D_{50}$) was 14.21 μm. The De Brouckere mean diameter, D (4, 3), and Sauter mean diameter, D(3,2) was 35.57 μm and 6.32 μm. Table 2 summarizes the chemical composition of cement, showing that CaO (58.34) and $SiO_2$ (26.83) are predominant constituents. Carbon dioxide (99% purity) was sourced from a gas company (Huanyu Jinghui Beijing), while laboratory tap water was utilized in the preparation of samples.

- Characterization of tailings

The morphological features of mine tailings were further examined using SEM with two magnification levels (× 300 and × 1000). The results showed that tailing particles are densely packed and exhibit a flaky, plate-like morphology with a distinct rough surface texture. They are highly heterogeneous, ranging from angular fragments to more irregular ones with sharp edges (Fig. 1). The observed geometry of tailings resembles that of past studies [55,56].

The fundamental physical properties are shown in Table 1. Sg was measured using a pycnometer (Le Chatelier flask method) ASTM D854-10 [57] and was determined to be 2.57, and the SS was determined by a Blain air permeability apparatus (Chinese standard GB/T 8074-2008 (GBT8074-2008) [58]) with a value determined as 476.14 $m^2$/kg, and the median particle size ($D_{50}$) was (49.2 μm). The chemical composition was evaluated using X-ray fluorescence (XRF-1800, Shemadu), and values are given in Table 2. The data shows that $SiO_2$ (60.13) and $Al_2O_3$ (17.82) are dominant in tailings. This composition is similar to previous studies [59–61].

The mineralogical analysis by a diffractometer (Bruker D8 AXS) showed that cement is mainly comprised of cementitious phases ($C_2S$ and $C_3S$), while tailings are predominantly composed of quartz along with other minerals such as clay, feldspar, and carbonates. The crystallinity of cement is 78.42%, while that of tailings is 82.67%, respectively, as shown in Fig. 2.

### 2.2. Recipe design and mix proportions

In this study, one control group with no $CO_2$ injection and the other nine $CO_2$-injected group specimens were prepared. Based on our previous experiments, a binder–to-tailing ratio of 1:6 after 3, 7, and 14 days of curing was chosen for a detailed study using a multi-functional chamber (Fig. 3) with controllable conditions (pressure, temperature, stirring, $CO_2$ injection rate, rotation etc.). To ensure data reliability, three identical specimens were prepared per group (n = 3), yielding 30 specimens across all injection duration groups and curing ages. All reported mechanical values are represented as the arithmetic means of triplicates. The mix design ratios are shown in Table 3. The samples were named based on their $CO_2$ injection duration and ratio as "mineralized-tailing based cement paste backfills, MTCPB injection time ratio." The temperature inside the reactor was maintained at 25°C, and the pressure was set at 0.5 MPa. The speed of the rotator was 800 rpm. For a better guarantee of slump, 75% concentration was maintained [62].

Fig. 3 shows the MTCPB preparation process. First, the raw materials were mixed mechanically in dry form using a paste mixer for about 5 min. Then, we introduced pre-determined laboratory tap water and again mixed for an additional five minutes to obtain a uniform consistency of paste. During the mixing process, $CO_2$ was allowed to enter the slurry from the base through a specially designed valve.

After the carbonation mixing of the slurry, it was poured into cylindrical plastic molds with a height of 100 mm and a diameter of 50 mm, adhering to the standard DZ/T 0276.18-2015 [63]. Prior to pouring of slurry, the molds were lined with an oil layer from the inside to avoid the sticking of the slurry to the walls of the mold. After pouring the slurry, the molds were gently tapped with a rod to remove the air bubbles from the slurry for proper compaction of the specimen. After waiting for one day, the specimens were demolded and then placed in the curing chamber immediately for optimal hardening, having a 20 ± 3°C temperature and 90 ± 2% humidity. Finally, the cured samples were tested after the designated curing days.

### 2.3. Methodology

#### 2.3.1. Strength test

The uniaxial compressive strength is a key indicator of the physico-mechanical properties of fill materials. It directly affects the stress and stability they can withstand during mining [64]. To investigate the effects of different processes on fill strength, a universal testing machine (UTM) was used on the basis of standard GB/T17671–2021 at a loading rate of 0.5 mm/min [65]. The machine can apply vertical stress and measure the corresponding stress and displacement. Prior to testing by UTM, the upper and lower edges of the cylindrical specimen were smoothened using sandpaper so that the load could be distribute uniformly. The height and width of the specimen were measured using a Vernier caliper. The stress/strain data and curves obtained from the computer system were processed. The UCS after each curing period was calculated as the average value of each triplicate test.

#### 2.3.2. SEM microstructural analysis

The SEM Zeiss SUPRA55 (Germany) with a resolution of 1 nm and an accelerating voltage of 20 kV was used for the internal microstructural observation of MTCPB combined with energy dispersive spectroscopy (EDS). This helped in observing the elemental distribution through energy distribution differences of the specimen for determination of physical phases in the samples. For SEM sample preparation, cubic-shaped pieces were selected after crushing the samples. The samples were placed in hydrated ethanol before the test to stop further hydration; otherwise, this effect the results. The specimens were then dried for 12 hours at 60°C for the removal of residual moisture and were coated with carbon for better electric conductivity. The samples were then mounted on specimen holders using conductive carbon tape. In short, the samples were retained in the SEM vacuum chamber and waited until the chamber was filled with vacuum prior to each experiment. The obtained SEM micrographs were digitally processed for a detailed understanding of the microtopography of the carbonized specimen. To establish a link between microstructural morphologies and strength behavior, specimens with different strengths were selected. Three specimens, MTCPB-0-1:6 (control group), MTCPB-10-1:6 (optimal group), and MTCPB-0-1:6 (prolonged carbonated group), were selected for detailed SEM experimentation. The aim of the SEM-EDS test was to understand the effects of carbonation injection on the strength behavior, compositional variations, interaction between $CO_2$ with tailings and cement, mineralization and carbonation dynamics of hydrated and carbonated products, carbonation-hydration mechanism,

**Table 1**
Physical specification of tested materials.

| Specifications | $^1D_{10}$ (μm) | $D_{30}$ (μm) | $^2D_{50}$ (μm) | $D_{60}$ (μm) | $D_{90}$ (μm) | $^3C_u$ | $^4C_c$ | Specific gravity | Specific surface area ($m^2$/kg) |
|---|---|---|---|---|---|---|---|---|---|
| Tailings | 6.37 | 20.61 | 49.2 | 99.43 | 203.45 | 14.76 | 0.34 | 1.47 | 476.14 |
| White cement | 2.24 | 7.72 | 14.21 | 61.43 | 289.73 | 12.34 | 0.24 | 1.13 | 1022.74 $m^2$/kg |

**Table 2**
Chemical composition tested materials.

| Constituents | $SiO_2$ | $Fe_2O_3$ | CaO | MgO | MnO | $P_2O_5$ | $Al_2O_3$ | $K_2O$ | $SO_3$ |
|---|---|---|---|---|---|---|---|---|---|
| Tailings | 60.13 | 4.42 | 4.78 | 1.87 | 0.11 | 0.28 | 17.82 | 6.44 | 0.53 |
| White cement | 26.83 | 0.73 | 58.34 | 0 | 0.28 | 0 | 10.32 | 0.387 | 4.34 |

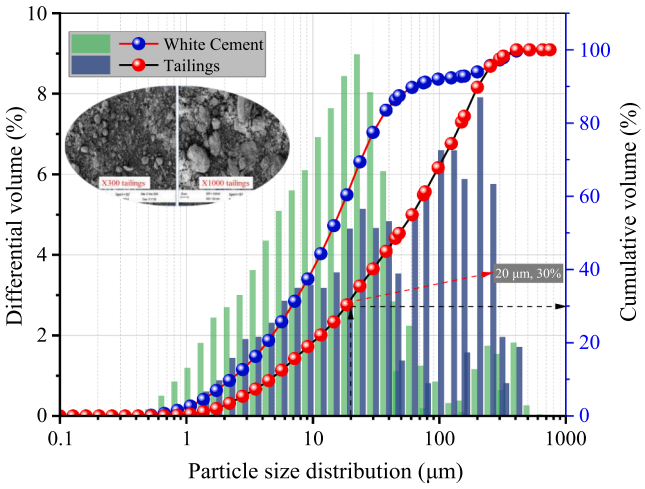



**Fig. 1.** Particle size distribution of raw materials.

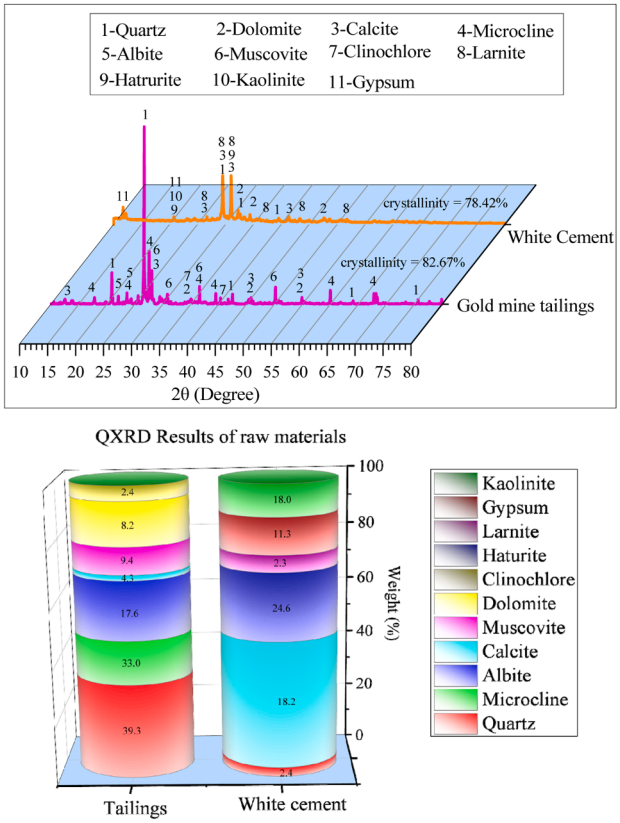



**Fig. 2.** XRD profile and QXRD results of raw materials.

microstructural evolution, and effects of synergistic effect of hydration-mineralization effects on the integrity of microstructures.

### 2.3.3. Carbon sequestration potential

Thermogravimetric analysis (TGA-DSC) was employed to quantify the carbon sequestration performance of MTCPB specimens by monitoring mass loss as a function of temperature at a defined heating rate. The samples for thermogravimetric analysis were prepared using the same procedure as for XRD characterization. To stop hydration and minimize the effect of particles on heat conduction, the samples were first ground to a fine powder with particles smaller than 75 μm. The powdered samples were then dried in a vacuum oven at 60°C for 48 hours to eliminate all free water, preventing any interference from moisture evaporation during the test.

The analysis was performed using a thermal analyzer, Netzsch STA 409PC. A small mass of MTCPB powder samples, approximately 30 mg, was heated from 30°C to 900°C at a rate of 10°C per minute under a nitrogen environment with a gas flow rate of 200 mL/min. To ensure complete decomposition at key stages during heating, three heating programs including three isothermal stages were selected: 15 min at 150°C to remove any residual moisture [66], 15 min at 550°C to facilitate full decomposition of hydroxides [35], and 30 min at 850°C to ensure complete breakdown of carbonates [52,53].

The selected temperature intervals for phase identification and quantification are grounded in well-established thermal decomposition signatures of cementitious phases reported in the literature. Specifically, temperatures below 200°C correspond to dehydration of free water, C-S-H gel interlayer water, and ettringite decomposition [66]. The interval of 390–500°C corresponds to the dehydroxylation of Portlandite ($Ca(OH)_2$), the primary reactive precursor in the carbonation reaction, whose characteristic peak position within this range is sensitive to the crystallinity and degree of carbonation [35]. The interval of 500°C –850°C corresponds to the decarbonation of $CaCO_3$ phases. This range is intentionally extended below the classical calcite decomposition temperature (~700–773°C) to capture the decomposition of poorly crystalline, amorphous, and metastable carbonate phases, including vaterite and aragonite that decompose across the broader 500–700°C range [52, 53]. By analyzing the mass loss within these defined temperature intervals, the carbon sequestration performance of MTCPB can be effectively quantified.

The $CO_2$ uptake attributed to accelerated carbonation was calculated using Equation (1):

$$\varphi(CO_2\%) = \frac{\eta_{550} - \eta_{850}}{\eta_{850}} \times \eta_{850}\,original \quad (1)$$

where: $\varphi(CO_2\%)$ is the $CO_2$ uptake attributable exclusively to accelerated carbonation, expressed as a percentage of the specimen mass. The $\eta_{550}$ and $\eta_{850}$ are the relative weight percentages of the carbonated MTCPB specimen at 550°C and 850°C, respectively, with their difference ($\eta_{550}-\eta_{850}$) representing the net mass loss in the 550°C–850°C interval corresponding to $CO_2$ released from all $CaCO_3$ phases. The $\eta_{850}$ original is the relative weight percentage of the non-carbonated control specimen (MTCPB-0-1:6) at 850°C, serving as the reference baseline correction factor.

The control correction via $\eta_{850}$ original is essential because without it, the raw mass loss in the 500–850°C interval would include three background contributions unrelated to accelerated $CO_2$ injection: (a) decomposition of intrinsic carbonate minerals naturally present in the raw tailings (confirmed by XRD); (b) background $CaCO_3$ from natural atmospheric carbonation during specimen preparation and handling; and (c) minor mass losses from non-carbonate tailings phases such as clay minerals and sulfates. By referencing against $\eta_{850}$ original, which embodies all three background contributions, Equation (1) isolates

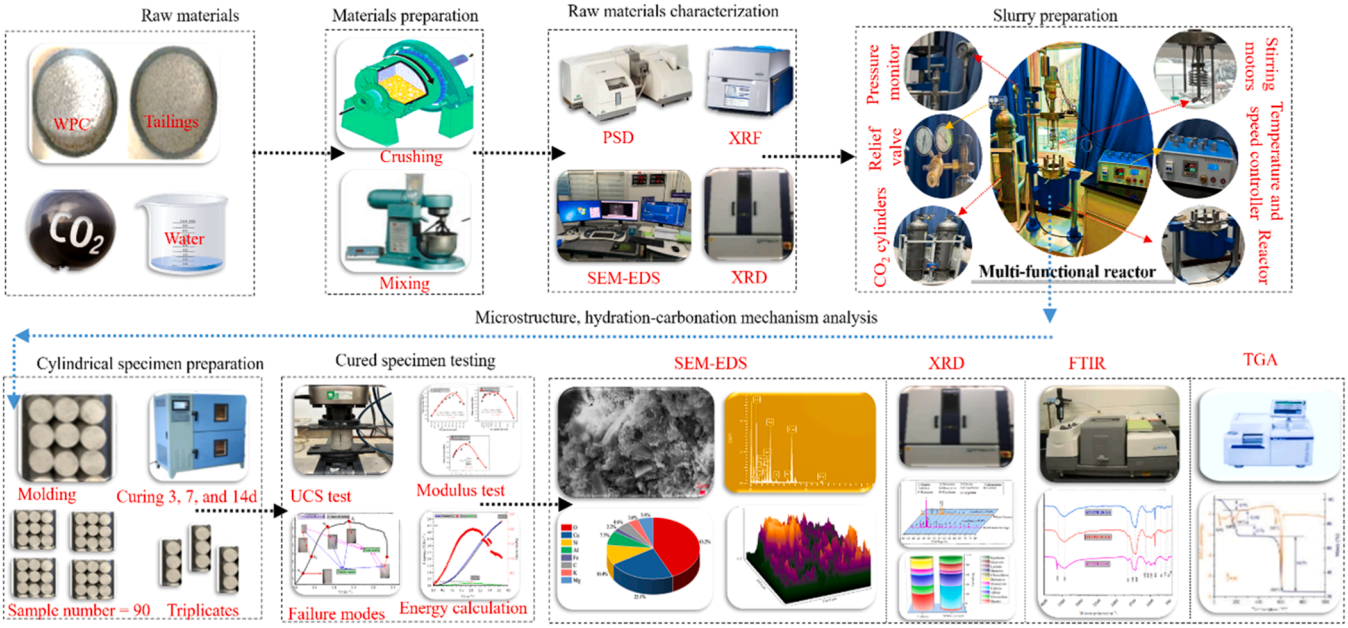



**Fig. 3.** Integrated methodology workflow for MTCPB study.

**Table 3**
Summary of MTCPB recipes in terms of $CO_2$ injection rates, cement-tailing ratio and solid mass concentration.

| Groups | Specimen | Injection time(min) | Stirring rate (rpm) | Cement/ Tails | Cure time | Conc. (%) | Tailings ($kg/m^3$) | Binders ($kg/m^3$) | Water ($kg/m^3$) |
|---|---|---|---|---|---|---|---|---|---|
| No-$CO_2$ integrated | MTCPB-0-1:6 | 0.00 | 800 | 1:6 | 3/7/14-days | 75 | 908.76 | 151.46 | 353.38 |
| $CO_2$- integrated | MTCPB-0.5-1:6 | 0.5 | 800 | 1:6 | 3/7/14-days | 75 | 908.76 | 151.46 | 353.38 |
| | MTCPB-01-1:6 | 01 | 800 | 1:6 | 3/714-days | 75 | 908.76 | 151.46 | 353.38 |
| | MTCPB-1.5-1:6 | 1.5 | 800 | 1:6 | 3/714-days | 75 | 908.76 | 151.46 | 353.38 |
| | MTCPB-02-1:6 | 02 | 800 | 1:6 | 3/714-days | 75 | 908.76 | 151.46 | 353.38 |
| | MTCPB-05-1:6 | 05 | 800 | 1:6 | 3/714-days | 75 | 908.76 | 151.46 | 353.38 |
| | MTCPB-08-1:6 | 08 | 800 | 1:6 | 3/714-days | 75 | 908.76 | 151.46 | 353.38 |
| | MTCPB-10-1:6 | 10 | 800 | 1:6 | 3/714-days | 75 | 908.76 | 151.46 | 353.38 |
| | MTCPB-15-1:6 | 15 | 800 | 1:6 | 3/714-days | 75 | 908.76 | 151.46 | 353.38 |
| | MTCPB-20-1:6 | 20 | 800 | 1:6 | 3/714-days | 75 | 908.76 | 151.46 | 353.38 |

exclusively the net $CO_2$ chemically fixed through direct $CO_2$ injection during slurry mixing.

#### 2.3.4. Fourier transform infrared spectroscopy (FTIR) analysis

FTIR is a widely used IR spectroscopy method. During the experimentation, light in the IR region is passed through the sample, which absorbs some quantity of energy while transmitting some amount. This emission and transmission of IR radiations is a unique property of each molecule [67]. The absorbed energy causes the vibration of molecules and gives information about the types of bonds present in them. It is often employed to analyze the reaction products of cementitious materials, which gives molecular fingerprints of the specimen, based on characteristics vibration types of the material [68]. For the determination of chemical structures of the carbonated/hydrated products, Attenuated Total Reflectance (ATR) FTIR was used in this current test based on the Chinese national standard BG/T 6040-2019 [69]. An FTIR infrared (NEXUS670) spectrometer was used with a resolution of 3 $cm^{-1}$, and wavenumber ranged from 400 $cm^{-1}$ –4000 $cm^{-1}$. During sample preparation, the test specimens were crushed to a fine powdered form to ensure intimate contact with the ATR crystal. Before analysis, the powdered sample was dried at about 60°C. The obtained data were then processed to identify different peaks (e.g., the carbonate $CO_3^{2-}$ band at ~1420 $cm^{-1}$ and the silicate bands between 900-1100 $cm^{-1}$) at various wavenumbers and intensities, showing the formation and vibrations of bonds in the samples. In this way, different compositions in the samples were identified.

## 3. Results and discussion

### 3.1. Uniaxial compressive strength development

Uniaxial compressive strength (UCS) is the paramount engineering property of cementitious backfill materials. This property specifies the load-bearing capacity and structural role of mine stability. This section describes the evolution of UCS in MTCPB as a function of $CO_2$ injection duration and curing age, examines the resulting trends, and develops a predictive model.

#### 3.1.1. Impact of $CO_2$ injection and curing duration on backfill strength

To investigate the effects of $CO_2$ injection duration on fill strength, a high-pressure reactor was used to evaluate the uniaxial compressive strength of MTCPB across varying $CO_2$ injection durations and curing ages e, as shown in Fig. 4.

The experimental results have shown that the UCS of MCPB was significantly regulated by $CO_2$ injection duration. With an increase in the $CO_2$ injection duration, the MTCPB exhibits a nonlinear trend of first increasing and then decreasing. The strength of MTCPB is maximized when the injection and stirring duration is 10 minutes, identified as optimal under the specific conditions investigated. This behavior is consistent with the cement strength theory and the proposed

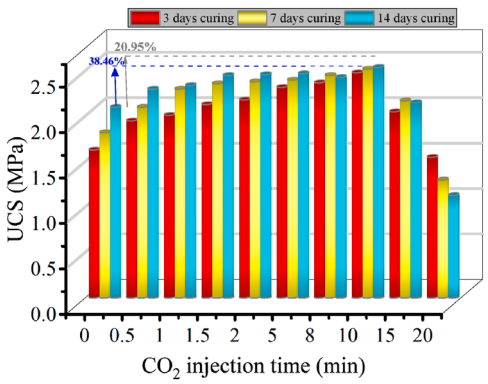



**Fig. 4.** Evolution of UCS with $CO_2$ injection at different days of curing.

mineralization reaction mechanism: hydration products are the main source of fill strength because they fill pores. However, the data suggest that they provide a relatively weak interlayer bond between cement and tailings particles, which may facilitate crack initiation during load application, thereby affecting the fill's microstructure and stability [56]. During the slurry mineralization process, $CO_2$ reacts preferentially with $Ca(OH)_2$ (Portlandite) to form $CaCO_3$ through direct carbonation. Simultaneously, a secondary carbonation pathway involves the decalcification of C-S-H gel, where $Ca^{2+}$ ions are extracted from the C-S-H structure to form additional $CaCO_3$, leaving behind a silica-rich amorphous gel ($SiO_2{\cdot}nH_2O$) as a residual phase. The $CaCO_3$ and silica-rich gel can connect free particles within the MTCPB and provide support, effectively enhancing the fill's interlayer bonding. This is consistent with the SEM-EDS observations reported in Section 3.8. It should be noted that $SiO_2$ observed in the system is a by-product of secondary C-S-H decalcification, not a direct product of $CO_2$ reaction, as confirmed by the FTIR bond analysis in Section 3.6.

When the aeration time exceeds 10 minutes, the strength of the MTCPB begins to decline. The data indicates that prolonged $CO_2$ reaction injection duration can negatively affect the strength of the fill. Excessive $CO_2$ causes expansion or degradation of the fill's internal pore structure, further affecting its overall mechanical properties. This over-mineralization damages the slurry's microstructure during the mixing stage, making it difficult to repair during subsequent curing. Therefore, the curing phase was unable to restore the structural defects caused by over-mineralization, leading to a decrease in MTCPB strength. In the later standard curing environment, additional $CO_2$ injection during the mixing phase dissipated during the initial curing period, and the internal pore structure gradually filled with hydration products. This made it hard for further $CO_2$ diffusion. Thus, the mineralization reaction slowed or even ceased. This behavior is consistent with SEM-EDS evidence in Section 3.8 that prolonged $CO_2$ exposure likely promotes progressive surface passivation, where dense $CaCO_3$ precipitation at pore entrances restricts further $CO_2$ diffusion into the matrix interior. This interpretation is supported by the Mg/Ca ratio inversion (reaching 12.46) observed in over-carbonated specimens, which is consistent with $CO_2$ starvation of the matrix interior under excessive injection conditions. The TGA data (Section 3.7) also shows that no net carbonate gain in over-carbonated specimens relative to the control is consistent with this interpretation of a self-limiting carbonation process under excessive $CO_2$ exposure.

For a more detailed study, the control group specimens, medium injection specimens, and prolonged injection specimens were selected after 14 days of curing.

An unexpected pattern was noticed for higher injections. The strength values of the control specimens were 2.07, 2.1, and 2.13 MPa, respectively. In the case of mineralized specimens, the strength initially rose from 0.5 min to 10 min of injection, reaching a peak of 2.54 MPa at MTCPB-10-1:6 after 14 days of curing and then declining at higher injections (MTCPB-20-1:6). This pattern at higher injections indicates that longer injections beyond the optimal window impede strength enhancement, pointing to an optimal duration of injection (MTCPB-10-1:6) to maximize strength and $CO_2$ uptake, as illustrated in Fig. 4. The data show that as the injection duration increases, more $CO_2$ fills voids and forms a passivation layer that halts further $CO_2$ into the backfill body [70]. This layer also affects the chemical process among cement minerals, tail particles, and entering $CO_2$. This composite matrix is characterized by distinct carbonated layers at outer and inner zones [71]. Thus, an intermediate injection duration (MTCPB-10-1:6) is required to attain the necessary strength of MTCPB while maximizing $CO_2$ uptake.

The observed rise in strength following $CO_2$ injection is due to the formation of $CaCO_3$ and other carbonated phases that contribute to the densification of microstructure and reduction of porosity, as corroborated by TGA, FTIR, and SEM-EDS results presented in Sections 3.6, 3.7, and 3.8, respectively. At the early curing age, the strength increase is primarily driven by hydration. For example, at 3 days of curing, the UCS fluctuated within +52.15% (i.e., from 1.63 MPa to 2.48 MPa) with varying injection time. For the medium- and long-term curing ages, the strength increase was significantly influenced by mineralization mixing. MTCPB-10-1:6 after seven days and MTCPB-10-1:6 after 14 days of curing showed strength increases of 38.46% and 20.95%, respectively, compared to the control group, as shown in Fig. 4.

### 3.1.2. *Impact of $CO_2$ injection duration on UCS trends*

UCS exhibits a clear non-monotonic dependence on the $CO_2$ injection duration, with a distinct maximum at 10 minutes across all three curing ages, as illustrated in Fig. 5. This overarching trend of progressive strength enhancement up to the optimal window followed by systematic decline beyond it reflects the competing effects of beneficial $CaCO_2$ densification at moderate carbonation intensity and detrimental surface passivation at excessive injection durations, as further discussed in Sections 3.6, 3.7, and 3.8.

At the control condition (MTCPB-0-1:6, 0 min), UCS values of 1.63, 1.82, and 2.10 MPa were recorded at 3, 7, and 14 days of curing, respectively, reflecting a purely hydration-governed strength development baseline. Specimens with short injection durations (MTCPB-0.5-1:6 through MTCPB-8-1:6) showed progressive but modest UCS improvements relative to the control, consistent with limited but increasing carbonation product formation. For example, MTCPB-0.5-1:6 showed a UCS enhancement of 9.52% relative to the control, while MTCPB-5-1:6 reached 17.62% above the control at 14 days, which suggests that brief injection durations generate insufficient carbonation products to substantially modify the pore structure, as confirmed by the SEM-EDS observations in Section 3.8.

Beyond the optimal window, UCS declined systematically. MTCPB-20-1:6 recorded an average UCS of 1.30 MPa at 14 days, a reduction of 46.19% relative to the control and 48.8% relative to the optimal condition. This marked degradation, despite the longest $CO_2$ exposure duration, is consistent with surface passivation restricting further $CO_2$ diffusion into the matrix interior, as discussed in Section 3.1.1 and supported by SEM-EDS stoichiometric evidence in Section 3.8. The data indicate that beyond the optimal threshold, additional $CO_2$ injection does not further enhance carbonation but instead generates microstructural heterogeneity that compromises mechanical integrity.

The standards for underground backfilling specify that the UCS of fill materials must lie between 0.2-5 MPa [72]. The test data show that UCS of all MTCPB specimens tested in this study falls within this prescribed range, confirming their suitability for underground backfilling applications across the full range of $CO_2$ injection durations investigated. Consequently, it can be deduced that under the specific experimental conditions of this study, a mineralization mixing duration of 10 minutes is recommended to balance mineralization efficiency and structural integrity of the fill. It is noted, however, that this optimal window is system-specific and may vary with binder type, tailings composition,

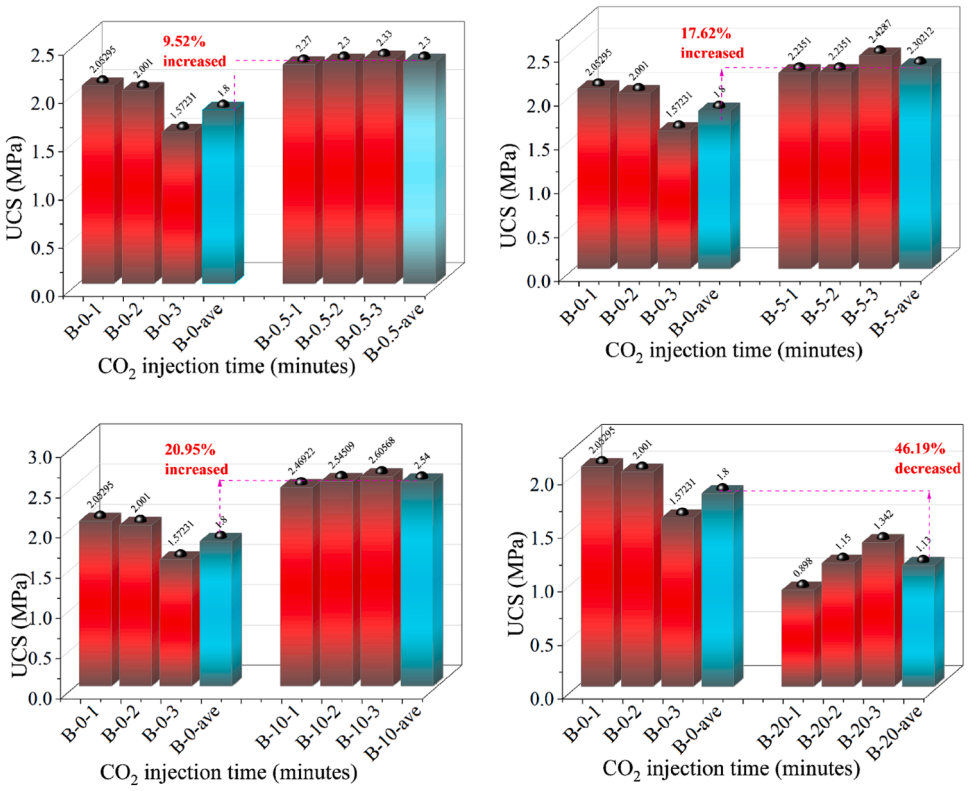



**Fig. 5.** Trend of UCS as $CO_2$ injection duration changes.

and reactor operating conditions.

### 3.1.3. *Impact of $CO_2$ injection duration on peak strain values*

Fig. 6 shows the variation in the peak strain values as the $CO_2$ injection duration into the filling slurry changes, highlighting the impact of the injection rate on the peak strain of the MTCPB samples. For a few samples, the magnitude of peak strain variation decreases with $CO_2$ injection duration, while for other samples, its value increases with carbonation time. For optimal values of injection, the specimens' tendency to resist the change in deformation during uniaxial compression

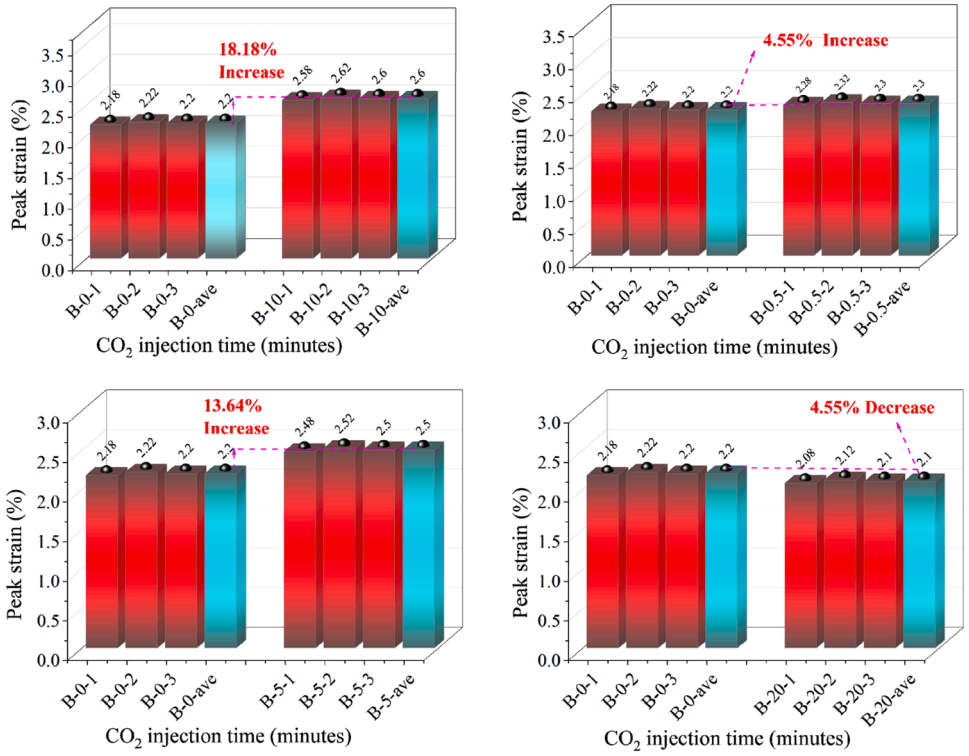



**Fig. 6.** Trend of peak strain as $CO_2$ injection duration changes.

increases for a small change in injection rate. The average results of these specimens confirmed that they have high internal pore development and are uniformly compacted. Consequently, the peak strain values decrease initially and then increase and reach a maximum value of 18.18% for the average value of MTCPB-10-1:6 as compared to the average peak strain value of the control group (2.2%). When the injection time is 0.5 minutes, the average peak strain value of the MTCPB-0.5-1:6 carbonated sample is increased by 4.55%. This means that the necessary hydration and carbonation reactions in this sample have not yet taken place, so the pore structures in the filling matrix and its compactness have not been developed in a good way. On the other hand, for 10 minutes of $CO_2$ injection (MTCPB-10-1:6 sample), the average peak strain value of all three samples (MTCPB-10-1:6-1, MTCPB-10-1:6-2, and MTCPB-10-1:6-3) increased by 18.8% as compared to the control group. This again shows that this is the optimal condition for $CO_2$ injection under these specific experimental conditions. In this case, $CO_2$ has entered into the matrix and provides space for more mineral carbonation reactions. For 20 minutes, that is, MTCPB-20-1:6 samples again, the average peak strain values decreased by 4.55% as compared to the average values of the control group (MTCPB-0-1:6-average) with a peak strain of 2.2%. These values further suggest that more $CO_2$ injection is not in favor of pore development and the compactness of the filling matrix.

#### 3.1.4. Predictive model for $CO_2$ injection and average UCS

For the quantitative evaluation of the relationship between average UCS and $CO_2$ injection duration, a predictive model was used. After using many models such as linear, quadratic, hyperbolic, and exponential/logarithmic, it was found that there is a non-linear relationship between average UCS and $CO_2$ injection duration. The quadratic function was selected to model the relationship because it shows the non-linear trend and directly identifies the optimal $CO_2$ injection duration and average UCS. The quadratic fitting equation is as under:

$$y = Ax^2 - Bx + C$$

Here, x is the $CO_2$ injection duration with different values, y is the UCS for different curing days, and the other are constants (A, B, and C).

The quadratic fitting relations are shown in Fig. 7 (a, b, and c). For 3 days of curing, the quadratic-fitted equation is $y = 1.8487 + 0.1321x - 0.00748x^2$ and $R^2 = 0.89$. For 7 days of curing, the quadratic fitted equation is $y = 2.0516 + 0.1275x - 0.00821x^2$ and in this case $R^2 = 0.903$ and finally, for 14 days of curing, the quadratic fitted equation is $y = 2.2134 + 0.1075x - 0.00796x^2$ with $R^2 = 0.954$. The greater the $R^2$ value, the more accurately the predictive model represents the data and the stronger the established correlation between $CO_2$ injection duration and UCS. From the trend of the quadratic fitted equation, it can be inferred that the line follows the quadratic function, and the trend of UCS growth is slower for 3 days and higher for 7 and 14 days due to the formation of more hydrated and carbonated products and the refinement of pores and overall fill structure. The trend also shows that 10 minutes of $CO_2$ injection with 14 days of curing is the optimum condition to achieve higher strength MTCPB fill materials.

### 3.2. Stress-strain response to carbonation intensity

The detailed evaluation of the elastic-plastic pattern of CPB is essential for studying its failure mechanism and mechanical characteristics [73]. The stress-strain curve functions as a mechanical fingerprint, revealing the internal fundamental damage mechanisms and failure evolution in backfill systems. While the uniaxial compressive strength quantifies the load-bearing capacity, the stress-strain curve morphology explains the deformation characteristics and damage progression that govern the structural performance of the materials. This section aims to analyze the systematic evolution of stress-strain characteristics across the complete spectrum of carbonation intensity (MTCPB-0-1:6 to MTCPB-20-1:6) at both early (7-day) and mature (14-day) curing stages. We also aim to develop a direct correlation between microstructural alternations and macroscopic mechanical responses. Furthermore, an "inverted-U" trend fundamental to carbonation optimization was

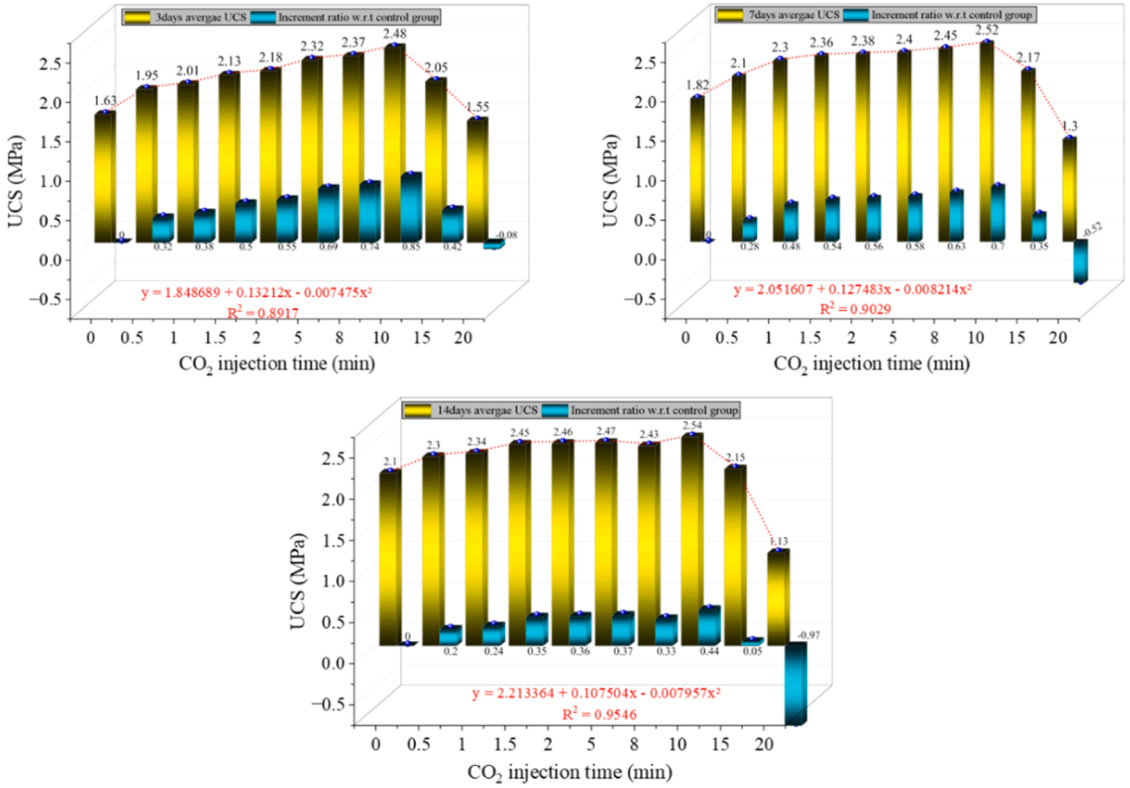



**Fig. 7.** Predictive models for different curing periods.

established, highlighting a critical threshold for beneficial carbonation.

On the basis of the stress-strain curve, the failure process of MTCPB is classified into six sequential stages (a, b, c, d, e), which are visually mapped on the curves and the corresponding specimen images in Fig. 8 and Fig. 9. Stage 1: pore-crack compaction (starting stage, 0 to 25% prior to peak stress). During this stage, the curve shows concave upward morphology, and there was no crack on the surface of the sample at this stage ($a_1$, $a_2$, $a_3$, $a_4$, and $a_5$) at both 7 and 14 days. Stage 2-stable crack evolution/linear elastic deformation stage marked at ($b_1$, $b_2$, $b_3$, $b_4$, and $b_5$), corresponding to 50% to 75% prior to peak stress. During this stage, the curve slope starts to decrease with an increase in stress, and stable micro-cracks develop within the fill body on the upper edge of the specimens. Furthermore, during this stage, axial strain and axial stress are linear. At this stage, although stresses concentration develops inside pores, they do not reach the failure threshold, and no any new cracks are formed.

Stage 3- plastic rupture formation stage and is also called the stage of non-stable development (75 to 100% prior to peak stress) and occurs at yielding points ($c_1$, $c_2$, $c_3$, $c_4$, and $c_5$). During this stage, unstable micro-cracks start to develop in the direction of tension, and the curve enters a convex shape. This stage plays a critical role in the stress level associated with crack propagation. Stage 4-peak point ($d_1$, $d_2$, $d_3$, $d_4$, and $d_5$) is characterized by further propagation of primary cracks and the emergence of tensile secondary cracks. This stage is most evidence under optimal conditions (10-min). Stage 5-post-breakage or post-peak failure stage ($e_1$, $e_2$, $e_3$, $e_4$, $e_5$) is characterized by continued expansion in tensile cracks with pronounced reduction in stress with increasing strain. Stage 6-loading end point ($f_1$, $f_2$, $f_3$, $f_4$, and $f_5$) marks the onset of macroscopic tensile failure. In this stage, cracks associated with failure spread across the sample surface, causing heavy damage. As a result, shear cracks develop and propagate along the shear failure planes and zones, which are ultimately responsible for the complete failure of the sample.

The stress-strain in Fig. 8 and Fig. 9 shows a pronounced morphological transformation with increasing $CO_2$ injection duration. These curves reveal three distinct behavioral regimes that correspond to microstructural evolution. The transition from hydration-dominated to carbonation-modified matrices alters deformation mechanisms from ductile pore collapse to brittle matrix fracture. The MTCPB-0-1:6 specimens exhibited classical quasi-brittle cementitious behavior, which is characterized by three distinct phases. The initial concave upward compaction stage (0-0.52% strain at 14 days) was particularly pronounced at 7 days of curing (Fig. 8**b**).

This indicates significant closure of capillary pores and micro-voids in the hydration matrix. This pore collapse mechanism dissipated substantial energy before the onset of linear deformation. The transition to peak strength occurred through stable microcrack propagation. This was followed by a gradual post-peak stress descent where a gradual load-bearing capacity was maintained. This residual strength resulted from frictional interactions along the newly formed fracture surfaces. After 14 days of curing (Fig. 9**b**), the overall stress-strain curve morphology was preserved. However, the initial compaction stage was shortened slightly, and the post-peak descent became more sharply defined. This evolution indicates maturation in the backfill matrix via ongoing hydration, which increases the inter-particle bonding. Despite this strengthening, the material's fundamental ductile failure mechanism remained unchanged.

In the moderate to optimal carbonation conditions (MTCPB-8-1:6 to MTCPB-10-1:6), carbonation fundamentally reshaped the deformation profile. Specimen MTCPB-8-1:6 represents a transitional state where the compaction phase shortened significantly (46% reduction compared to MTCPB-0-1:6 at 14 days). This phenomenon indicates the partial pore filling process due to carbonation products, which are confirmed by SEM-EDS images. The linear elastic region became more pronounced. The increased slope was directly correlated with matrix stiffness. Notably, MTCPB-10-1:6 shows dramatic transformations. In this instance, the compaction stage reduced to 0.21% strain after 14 days of curing (Fig. 9**d**). This slight compaction demonstrates that compressible porosity has been almost entirely removed due to precipitation of $CaCO_3$ filling the pores [35].

The elastic region extended approximately 70-75% of the peak stress. This again shows the transformation to elastic behavior predominantly. Minor stress fluctuations (0.5-1.6% amplitude) were detected consistently in MTCPB-10-1:6 specimens just before reaching peak stress during both curing ages. These perturbations represent a sequence of micro-crack initiation and subsequent arrest. The arrest mechanism is facilitated by a carbonate bridging mechanism, where $CaCO_3$ crystals span the micro-cracks. In this process, the carbonate crystals that span the micro-cracks temporaryily halt propagation. Fractures proceed only after sufficient energy accumulates to break these bridges [34]. The post-peak response transformed markedly. A gradual stress decay was replaced by an abrupt reduction. The slope of this descent increased by approximately three times compared to MTCPB-0-1:6, indicating a clear transition in the failure mechanism from ductile to brittle fracture.

After an optimal value of $CO_2$ content, these carbonation effects were no longer beneficial. MTCPB-15-1:6 exhibited inconsistent curve shape, non-linear compaction characteristics at a strain value of 0.35%, and instances where there were various yield points. This observation suggests a heterogeneous carbonation distribution that creates zones of differing stiffness. For MTCPB-15-1:6 (Fig. 8**e** and Fig. 9**e**), the post-peak drop is more abrupt but less consistent than for MTCPB-10-1:6. For specimen MTCPB-20-1:6, there was a significant loss of mechanical performance. In its loading phase, it failed to show linearity on several occasions due to possible damage. The unique characteristic of this specimen was that once it had attained maximum stress, it failed abruptly. This is a graphical representation of the explosive disintegration observed in laboratory testing. Such behavior indicates a fundamental loss of cohesive strength and the existence of critical flaws that facilitate rapid, unstable crack propagation [74].

The curing time significantly affected how carbonation affected the stress-strain relation of the specimens. After 7 days of curing (Fig. 8), the curves demonstrated the same trend as previous observations, with a less defined curve, wider compaction stages, and smoother transitions between stages of strain. In addition, the carbonation effect was observable but not as pronounced as before; the typical yield-point fluctuation was less noticeable, and the slopes after the peak were less inclined. By day 14 (Fig. 9), the characteristic properties of each different carbonation level began to manifest themselves clearly. While the specimen with MTCPB-0-1:6 maintained its ductility and revealed elastic separation, the MTCPB-10-1:6 was characterized by yield point fluctuation and sharp inclination after the peak. The MTCPB-20-1:6 (Fig. 9**f**) specimen was significantly degraded and featured numerous irregularities during loading. This observation implies that because of hydration, the cementitious matrix forms around the carbonate matrix and enhances its inherent behaviors established due to early carbonation. With regard to a well-carbonated matrix (MTCPB-10-1:6), the latter becomes stiff and brittle (Fig. 9**d**); however, a poorly carbonated matrix (MTCPB-20-1:6) becomes strong but flawed (Fig. 9**f**).

Unlike studies [73,75], there are several notable insights from this study. First, it shows a well-defined relationship between strength and ductility such that longer $CO_2$ exposure leads to a reduced UCS while increasing the ultimate failure strain. Second, longer curing periods increase the strength of uncarbonated cylinders, while for carbonated samples, the major contribution lies in increased toughness and deformability. Third, the basic modes of failure have not changed due to these differences in mechanical behavior. It is noted that failure always starts with tensile cracking followed by shear localization, regardless of the curing period and levels of carbonation. Carbonation influences the mechanical properties of the materials; however, the modes of failure remain constant. Finally, under the conditions investigated, the optimal performance balance was observed for ten minutes of $CO_2$ exposure and fourteen days of curing, leading to strength retention of more than 2 MPa and ductility of 3.5% strain.

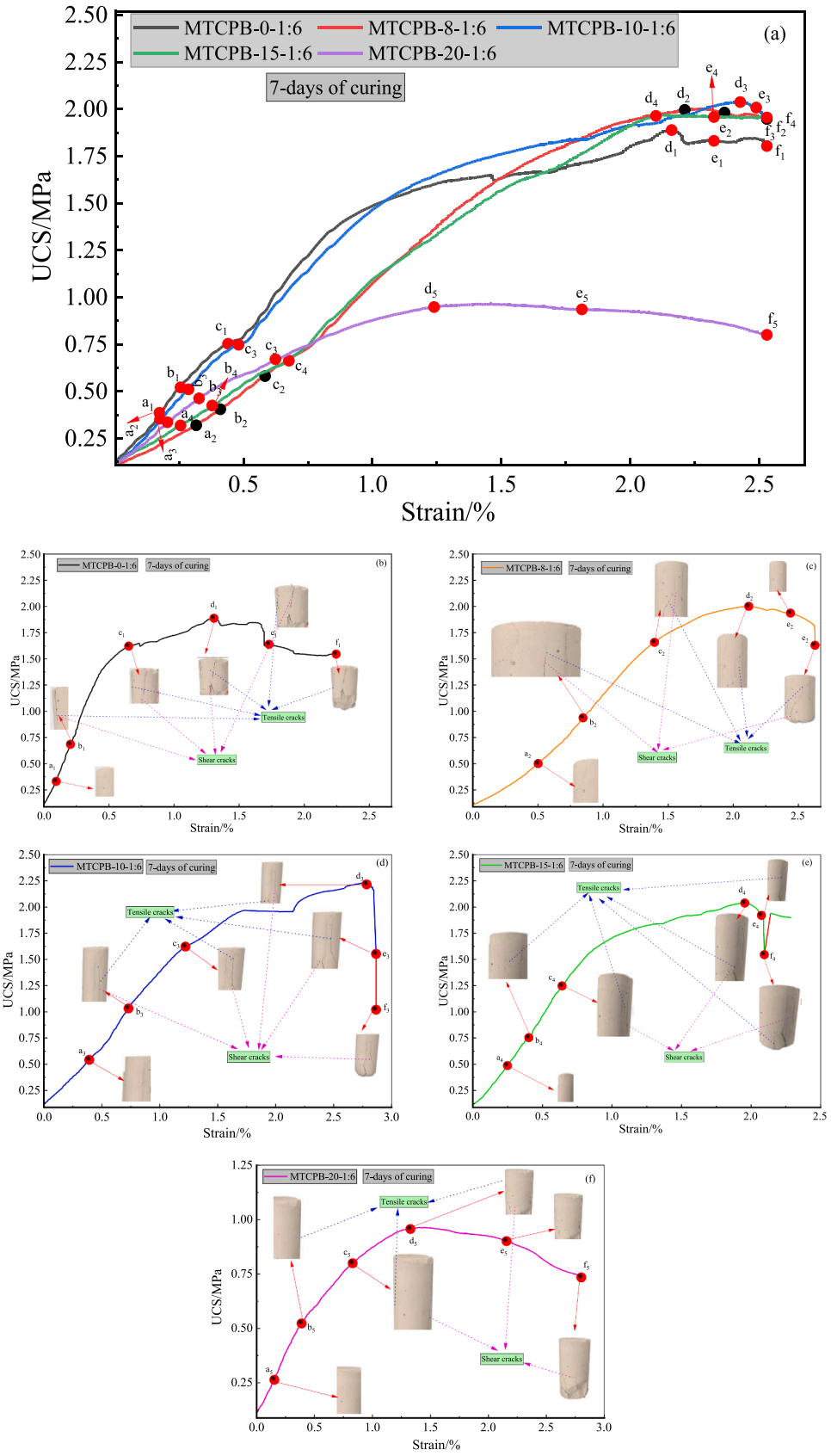



**Fig. 8.** (a) Complete stress-strain responses for all carbonation levels at 7-days (b) control group (c) moderated carbonation (d) optimal carbonation (e) over carbonation (f) excessive carbonation.

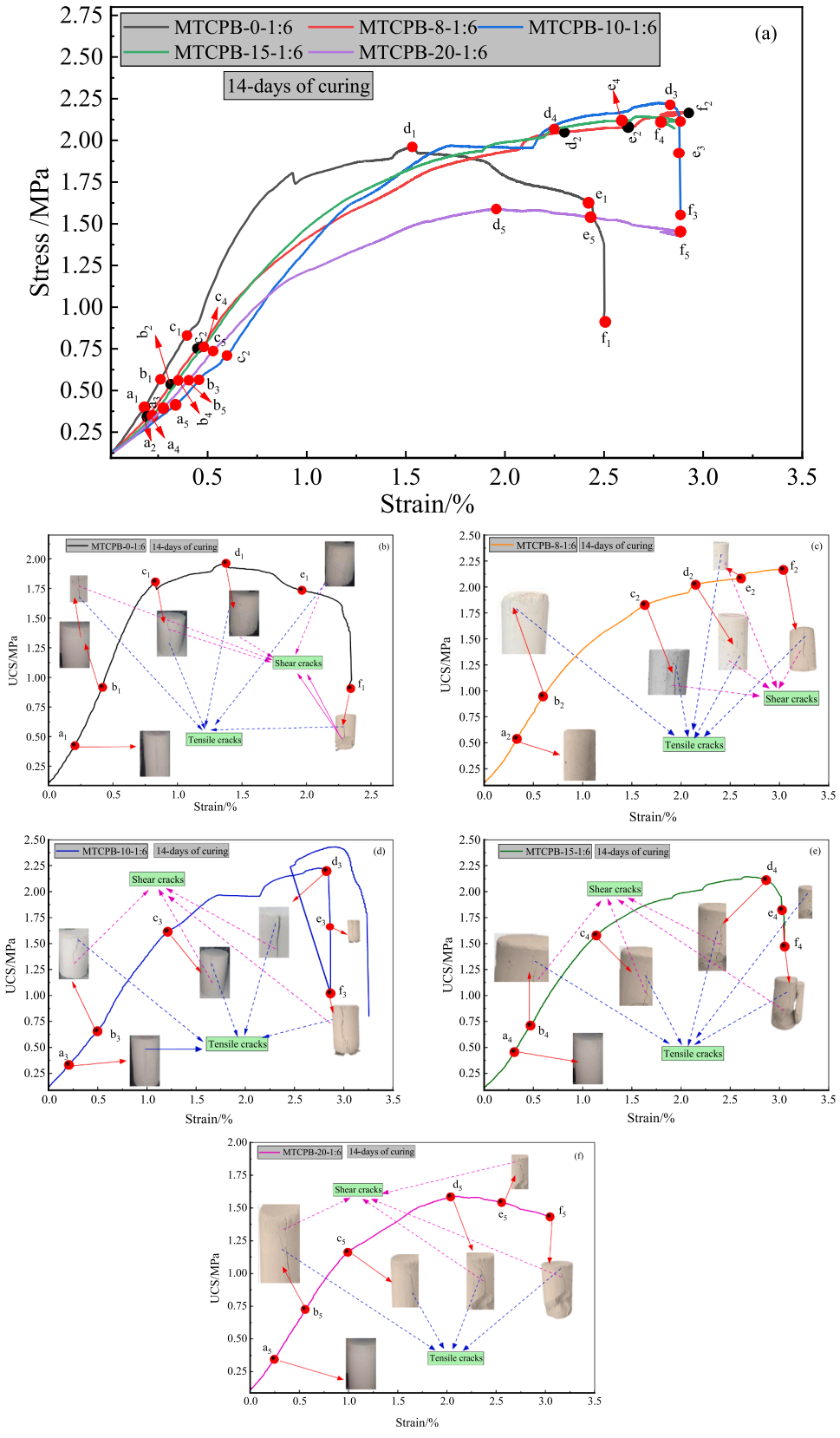



**Fig. 9.** Comparative stress-strain curve with failure modes of MTCPB specimens at 14-days (a) Full curve (b) control group (c) moderated carbonation (d) optimal carbonation (e) over carbonation (f) excessive carbonation.

### 3.3. Failure modes and fracture mechanism evolution response to $CO_2$ injection

CPB is an inhomogeneous material with multiple phases, which consists of intrinsic defects like air pores, pre-cracks, and micropores. Under compressive stress, these initial defects will be closed, stretched, and eventually interconnected, a sequence that dictates the failure mechanism of CPB [76]. Backfill materials can fail in several ways, including tensile failure, shear failure, and mixed failure [77]. This section highlights how $CO_2$ injection duration plays a vital role in altering the damage development process, changing failure mechanisms from shear and tensile to fragmentation. The systematic variation in macroscopic fracture pattern across various curing ages provides direct visual evidence of the microscopic evolution (pore refinement, $CaCO_3$ formation), as documented in the SEM-EDS images in Section 3.8. This establishes a direct structure-property relationship and a comprehensive failure taxonomy of the material and helps in linking the visible crack morphologies to the related mechanical behavior.

The failure modes of MTCPB specimens evolve systematically with both $CO_2$ injection duration and curing age, as shown in Fig. 10 and Table 4 (7 days of curing) and Fig. 11 and Table 5 (14 days of curing). These figures present the final failed states of all specimens.

The progression in failure modes can be classified into three distinct regimes, such as shear-dominated, tensile-dominated, and mixed/disintegrated. Each regime directly correlates with specific stress-strain behaviors and microstructural states. This classification is based on the dominant crack type and pattern moving from a state of distributed damage to localized fracture and finally to disintegration.

Regime I-shear dominated failure (MTCPB-0-1:6): the non-carbonated control specimens failed via a classic shear mechanism characterized by fracture planes. At 7 days of curing (Fig. 10**a**), MTCPB-0-1:6 exhibited conjugated shear failure with multiple intersecting inclined crack planes (~55-65°) forming a pronounced "X" pattern. This fracture geometry indicates a matrix with homogeneous weakness distribution. This allows cracks to propagate along planes of maximum shear stress through the weakest interfacial transition zones (ITZs) between tailings and cement hydrates. By 14 days (Fig. 11**a**), the failure refined to a single dominated shear plane with minimal secondary cracking. This reflects increased matrix homogeneity due to continued hydration that creates more uniform weak paths. The abundance of mirocracks at 7 days and their consolidation at 14 days correlate with the material's evolving porosity and their gradual, ductile post-peak response.

Regime II-transition to tensile dominated failure (MTCPB-8-1:6, MTCPB-10-1:6): Carbonation brings about a relatively clear change in the fracture regime from a predominantly shear to mostly tensile failure mechanism. After 7 days (Fig. 10 **(b, c)**) the behavior of MTCPB-8-1:6 represents transitional mixed-mode failures characterized by a

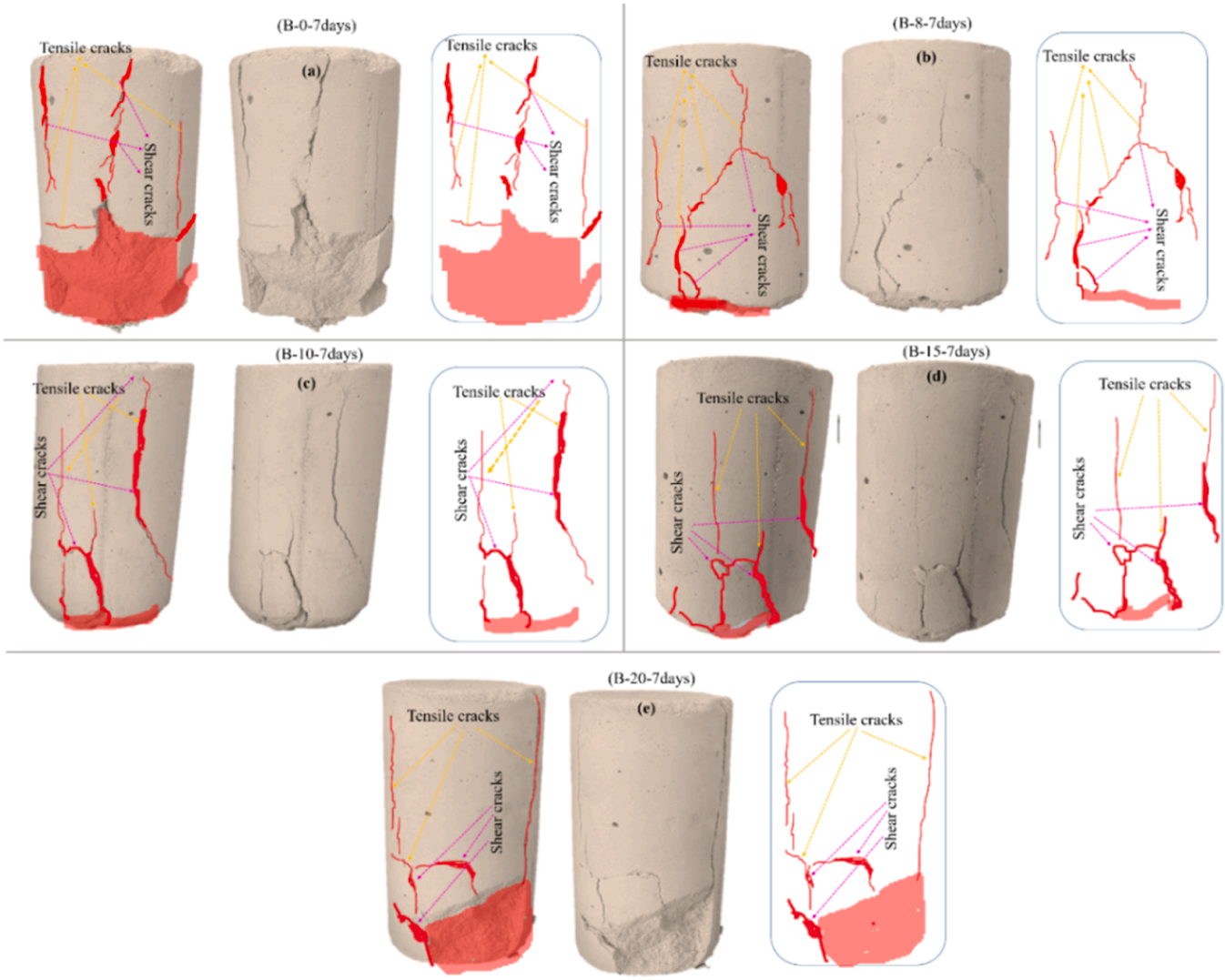



**Fig. 10.** Macroscopic failure modes of MTCPB after 7 days of curing.

**Table 4**
Failure mode characteristics of MTCPB at 7 days of curing.

| Specimen | $CO_2$ injection (min) | Dominant crack type | Fracture pattern description | Fragment count | Spalling severity |
|---|---|---|---|---|---|
| MTCPB-0-1:6 | 0 | Shear (conjugate) | Multiple intersecting inclined planes (~60°) forming "X" pattern. Distributed microcracking | 4-6 | medium |
| MTCPB-8-1:6 | 8 | Mixed mode | Primary inclined shear crack with secondary vertical tensile cracks. Clear transitional hybrid pattern | 3-5 | medium |
| MTCPB-10-1:6 | 10 | Tensile (axial split) | Clear vertical splitting, 1-2 dominant cracks with minimal lateral branching | 2-3 | low |
| MTCPB-15-1:6 | 15 | Mixed fragmentation | Multi-directional intersecting cracks (shear & tensile). Several irregular fragments | 4-7 | high |
| MTCPB-20-1:6 | 20 | disintegrative | Shattered appearance, loss of cylindrical form, severe surface spalling and pulverization | ≥ 8 | Very high |

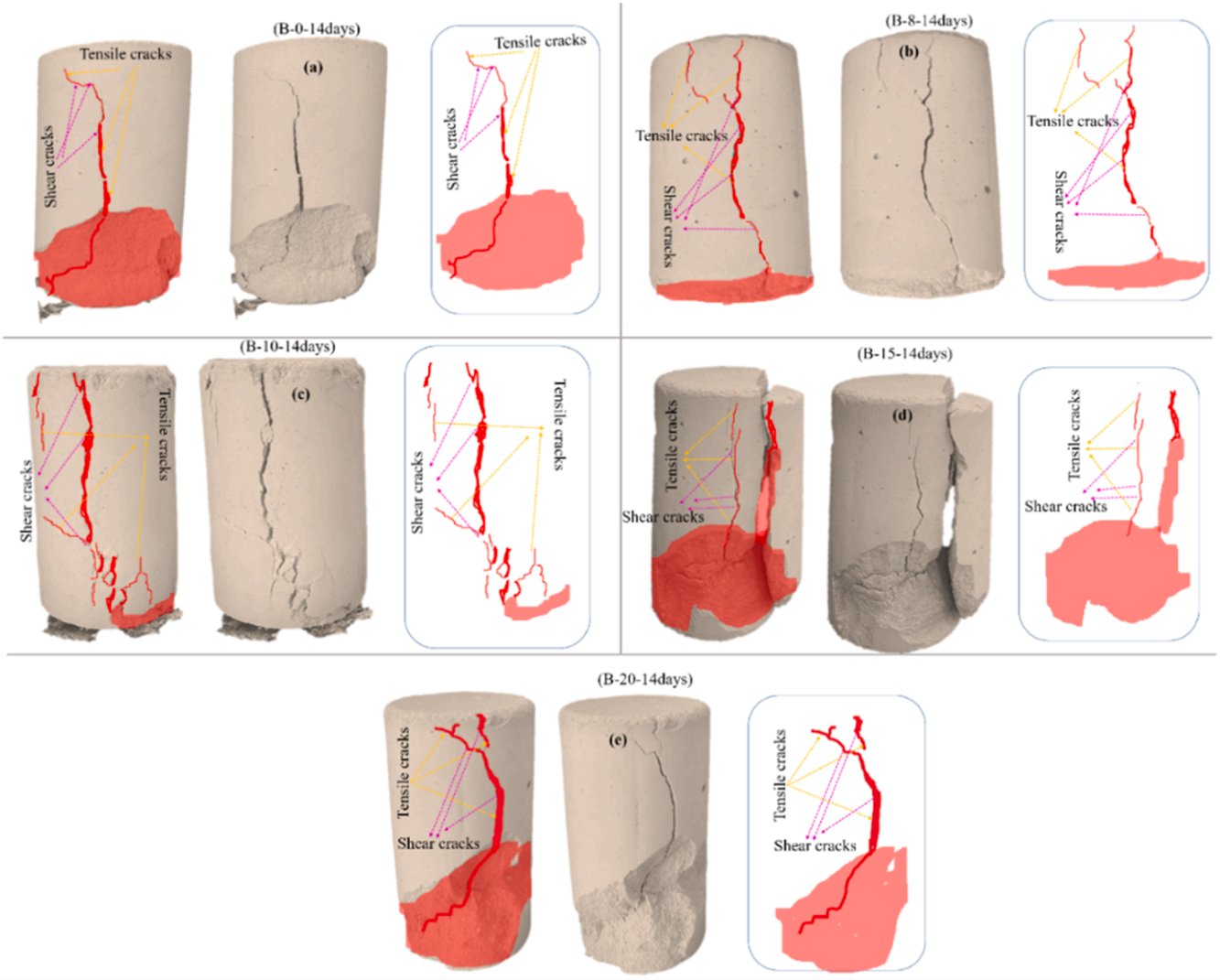



**Fig. 11.** Macroscopic failure modes of MTCPB after 14 days of curing.

primary crack inclined (shear) accompanied by a secondary vertical (tensile) crack developing from stress concentration points. Such mixed-mode failure is an indication of incomplete matrix strengthening where the interfaces have been strengthened by carbonation but not enough to change the fracture behavior. However, after 14 days of curing (Fig. 11 (**b, c**)), there is a marked shift in failure behavior of MTCPB-8-1:6 from shear to tensile splitting. MTCPB-8-1:6 (optimum carbonation) failed predominantly due to axial tensile splitting cracks. Such failures occur vertically, are through thickness in nature, and do not spread horizontally. This implies a change in the failure mechanism, which can be attributed to the interface strengthening by carbonate bonds. Therefore, the cracking occurs in the matrix material instead of along the particle interfaces. Lateral tensile stresses caused by Poisson's expansion will be determined by the tensile strength of the strengthened matrix. This will consequently result in vertical splitting [39]. This change in the failure mechanism is due to the increase in the connectivity and efficiency of carbonate bonds formed due to the precipitation of $CaCO_3$.

**Table 5**
Failure mode characteristics of MTCPB at 14 days of curing.

| Specimen | $CO_2$ injection (min) | Dominant crack type | Fracture pattern description | Fragment count | Spalling severity |
|---|---|---|---|---|---|
| MTCPB-0-1:6 | 0 | Shear (single) | Single dominated inclined plane (~60°), minimal secondary cracking, cleaner fracture surfaces | 2-3 | Low-medium |
| MTCPB-8-1:6 | 8 | Tensile-leading | Dominant vertical split, very few secondary cracks, clear progression from mixed mode at 7 days | 2-4 | Low-medium |
| MTCPB-10-1:6 | 10 | Tensile (defined split) | Singular, clean vertical fracture, very few secondary cracks, optimal crack localization | 2 (primary) | low |
| MTCPB-15-1:6 | 15 | Severe fragmentation | Increased fragment count, more complex crack network, enhanced brittleness | 5-8 | High-very high |
| MTCPB-20-1:6 | 20 | Catastrophic disintegration | Complete loss of specimen integrity, fine fragments, explosive failure morphology | ≥ 10 | extreme |

Regime III-mixed fragmentation to disintegrative failure (MTCPB-15-1:6, MTCPB-20-1:6): Beyond the optimal conditions, excessive and over $CO_2$ injection degrades structural coherence through mixed-mode fractures. MTCPB-15-1:6 fails through multi-dimensional fragmentation (Fig. 10**d** and Fig. 11**d**), with intersecting shear and tensile crack networks creating several irregular fragments. This complex mixed pattern indicates heterogeneous carbonation distribution, creating zones of differential strengths and brittleness. Due to this, multiple independent cracks initiate, which interact unstably. The MTCPB-20-1:6 exhibited catastrophic disintegration and lost its cylindrical form entirely. The 14 days specimen (Fig. 11**e)** shows more extreme shattering and loss of form than the 7 days curing specimen (Fig. 10**e**). This over-carbonated specimen shattered into numerous small fragments through simultaneous shear and tensile failure with extensive surface spalling. This explosive mixed-mode failure morphology shows the simultaneous activation of multiple critical flaws from micro-cracking between over-carbonated crusts and under-reacted cores combined with weak interfacial zones. Such disintegration represents the instantaneous release of stored elastic energy through unstable mixed-mode crack coalescence, corresponding directly to vertical stress drops in the MTCPB-20-1:6 stress-strain curve.

A direct comparison of specimens between 7 and 14 days of curing (Fig. 10 and Fig. 11) showed that in addition to $CO_2$ injection duration, the curing duration systematically modified the crack morphology within each carbonation regime. For all specimens of 14 days curing produces more defined and severe crack patterns, such as cleaner shear planes in the control group (MTCPB-0), which are more pronounced and isolated tensile splits in the optimal group (MTCPB-10) with reduced secondary cracks and more violent fragmentation with mixed-mode cracks in the excessive carbonation specimen (MTCPB-15) and over-carbonation specimen (MTCPB-20).

The failure progression in MTCPB follows mechanisms known for cemented composites. The researchers in the former study observed stages that are similar to the formation of cracks due to external loads on lepidolite tailings [73]. Another study also observed similar mechanisms of failure in conventional CPB [78]. The present study, however, shows that controlled $CO_2$ injection can actively optimize failure modes and improve related mechanical characteristics. This relationship has not been widely examined in previous backfill studies.

### 3.4. Elastic modulus variation

The elastic modulus of cement paste backfill (CPB) is a critical design parameter that represents its stiffness and resistance to elastic deformation under applied load [34]. For CPBs, the values of E range from 100 MPa to 2000 MPa depending upon the composition of raw materials used in CPB preparation, curing conditions, microstructure evolution, etc. Increasing the cement content and curing age promote hydration, making more cementitious gels (C-S-H) that densify the matrix and significantly increase the stiffness [54]. A high water-to-cement ratio (w/c) increases the capillary pores, creates more voids and weaker points, and thus reduces E [79]. Higher solid contents (lower water) generally increase E. CPBs cured under simulated in-situ stress (drained or undrained) develop a higher modulus than unconfined samples due to particle rearrangement and reduced void ratio [34]. This is critical for realistic design. The lab-designed unconfined tests can underestimate in-situ E by 2-5 times [80]. Higher loading rates increase measured E. Curing at higher temperatures accelerates hydration that leads to higher early age E but causes micro cracking from thermal stress at later ages. The elastic moduli can be predicted over time using mature models (based on time and temperature history), especially from blended binders.

In this study on MTCPB, the elastic modulus of the specimen increased with curing time, just like the increasing trend of UCS development, but with different values. Fig. 12 and Table 6 shows the variations in elastic modulus with increasing $CO_2$ injection duration. The modulus increases by 26 MPa at 0.5 minutes, 31 MPa at 1 ', 40 MPa at 1.5 minutes, and 44 MPa at 2 minutes as compared to the control group (130 MPa at 3 days). Under the specific conditions investigated, the optimum carbonation (10-minute injection) enhanced the modulus by 68 MPa to reach 198 MPa, representing a 52% improvement. In contrast, over carbonation (20 ' injection) yields only 124 MPa, which is 6 MPa lower than the control group and 74 MPa lower than the optimum. This also shows the detrimental effects of over carbonation. These values of E show a clear optimum condition for the performance of MTCPB under the conditions investigated, where moderate carbonation significantly strengthens the matrix while prolonged injection degrades stiffness. This is consistent with the surface passivation mechanism discussed in Section 3.1.1 and supported by SEM-EDS evidence in Section 3.8.

The elastic modulus predictive equations for the three curing ages are presented in Fig. 12 (**a, b, c**) with full statistical parameters such as adjusted $R^2$, Prob > F, and RMSE, summarized in the inset table of each panel. The fitted equations are as follows. For the 3-day curing specimen (Fig. 12**a**), the elastic modulus follows a cubic relationship with injection time: $E(x) = 129.2 + 8.2x + 1.323\,x^2 - 0.180\,x^3$ ($R^2 = 0.909$), where x represents the injection time in minutes. This cubic function captures the initial rapid enhancement (0-8 minutes), peak performance (8-10 minutes), and subsequent decline (10-20 minutes) characteristic of early-age carbonation. For 7 d cured specimens (Fig. 12**c**), the optimization adopts a Gaussian distribution: $E(x) = E(x) = y_o + A/[w\sqrt{(\pi/(4\ln 2))}] \times \exp[-4\ln 2(x-x_c)^2/w_2]$ ($R^2 = 0.933$). It can be seen that the Gaussian model shows an optimal injection duration of 7.47 ± 0.45 minutes with a peak modulus of 227 MPa observed at 10 minutes. The broad width parameter (w = 17.3 minutes) indicates a significant stiffness enhancement occurs across a wide injection range (approximately 0-15 minutes). By 14 days of curing (Fig. 12**b**), the relationship between E and injection time changes to simplified quadratic form: $E(x) = 230.0 + 11.23\,x - 0.828\,x^2$ ($R^2 = 0.954$). This quadratic model predicts maximum stiffness of 268 MPa at 6.78 minutes of injection. This shows an enhancement of 16.6% over the control specimen (230 MPa). The experimental validation confirms sustained high performance (> 250 MPa) from 5 to 15 minutes of injection duration. All three models

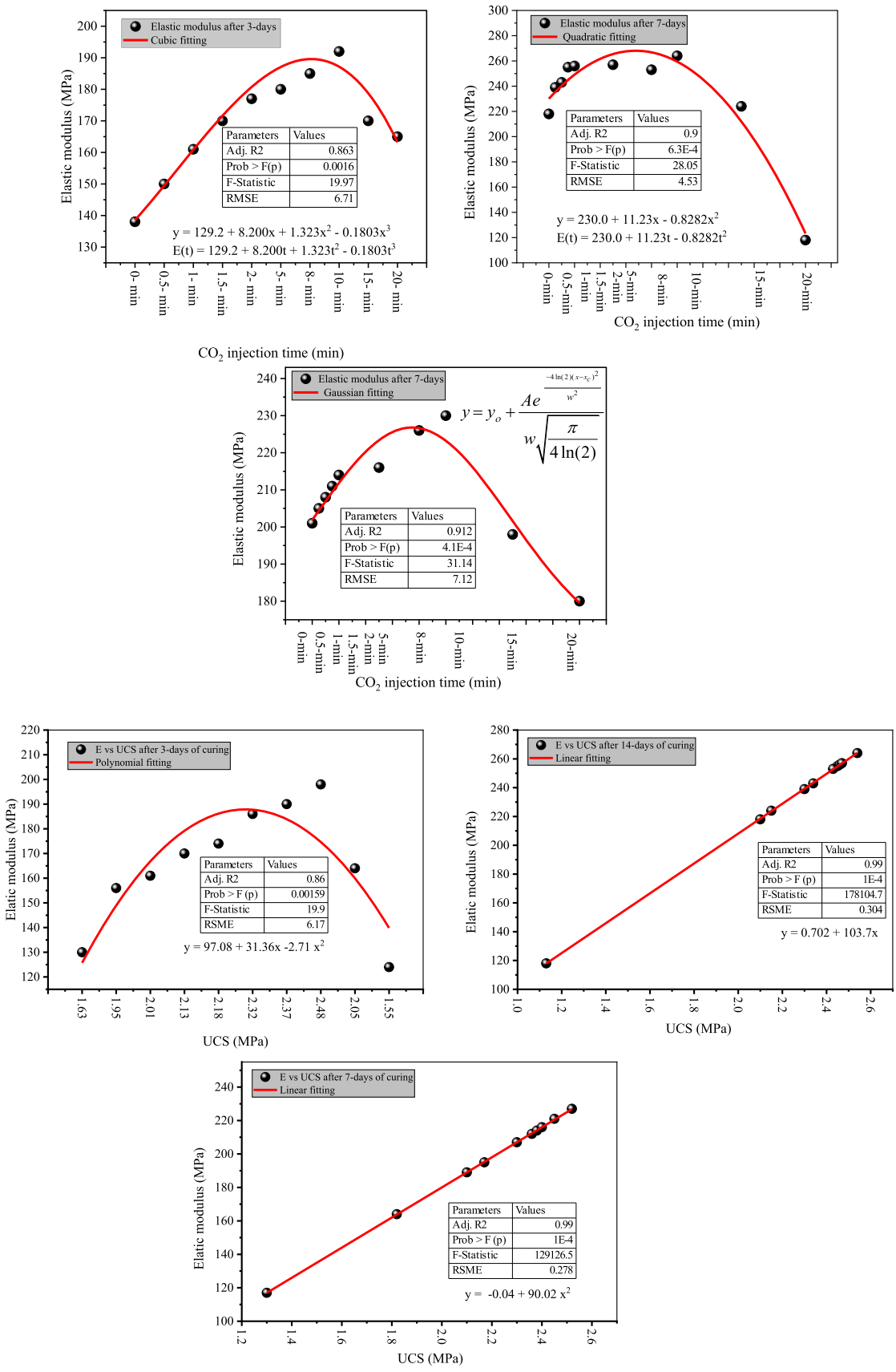



**Fig. 12.** Predictive models correlating elastic moduli, $CO_2$ injection duration and UCS at various curing periods.

**Table 6**
Evolution of UCS and elastic moduli with injection times.

| Specimen | Injection time(min) | 3 Days Curing UCS (MPa)/E (MPa) | 7 Days Curing UCS (MPa)/E (MPa) | 14 Days Curing UCS (MPa)/E (MPa) | Total E increase 3 →14 days |
|---|---|---|---|---|---|
| MTCPB-0-1:6 | 0 | 1.63/130 | 1.82/164 | 2.10/218 | +67.7% |
| MTCPB-0.5-1:6 | 0.5 | 1.95/156 | 2.10/189 | 2.30/239 | +53.2% |
| MTCPB-01-1:6 | 01 | 2.01/161 | 2.30/207 | 2.34/243 | +50.9% |
| MTCPB-1.5-1:6 | 1.5 | 2.13/170 | 2.36/212 | 2.45/255 | +50.0% |
| MTCPB-02-1:6 | 02 | 2.18/174 | 2.38/214 | 2.46/256 | +47.1% |
| MTCPB-05-1:6 | 05 | 2.32/186 | 2.40/126 | 2.47/257 | +38.2% |
| MTCPB-08-1:6 | 08 | 2.37/190 | 2.45/221 | 2.43/253 | +33.2% |
| MTCPB-10-1:6 | 10 | 2.48/198 | 2.52/227 | 2.54/264 | +33.3% |
| MTCPB-15-1:6 | 15 | 2.05/164 | 2.17/195 | 2.15/224 | +36.6% |
| MTCPB-20-1:6 | 20 | 1.55/124 | 1.30/161 | 2.13/118 | -4.8% |

confirm Prob > F < 0.0001, establishing statistical significance across all curing ages.

The transition in mathematical form from cubic (3-day curing) to quadratic (14-day curing) shows evolving carbonation-hydration interactions. Early age (cubic) shows complex interaction and then stabilized optimization (Gaussian) and finally the fundamental competition between beneficial and detrimental effects (quadratic). This progression suggests that carbonation initially creates heterogeneous microstructures that are gradually homogenize with time.

The increase in elastic modulus as compared to the control group (0-minute injection) varies with curing time from 3 days to 14 days. At 3 days of curing, under the experimental conditions of this study, optimal carbonation (10 minutes) increases stiffness by 52% (130 to 198 MPa). By 7 days of curing, this enhancement reduces to 38% (164 to 227 MPa), and at 14 days of curing, it further decreases to 21% (218 to 264 MPa). This reduction trend with curing days shows that carbonation provides high early-age acceleration and long-term stiffness increase and is dominated by carbonation products. However, over carbonation effects become more prominent with the increase in the $CO_2$ injection duration ($\geq$ 15 minutes). At 20 minutes of injection, the elastic modulus decreases to 124 MPa (3 days), 117 MPa (7 days), and 118 MPa (14 days). This trend shows a reduction of 37%, 49%, and 55%, respectively, as compared to the optimal conditions. This stiffness degradation is consistent with microstructural observations showing pore blockage and uneven carbonate distribution under excessive $CO_2$ exposure, as shown in SEM-EDS section Fig. 12.

### 3.5. Energy distribution assessment

It has been established by researchers that energy change is the fundamental mechanism governing the change in physical properties of materials and helps in quantifying fracture performance and microstructural changes. The total energy (or toughness) per unit volume is calculated as the total area under the entire stress-strain curve [81]. The elastic energy represents the reversible energy stored under the unloading path in a cyclic loading test. The slope of this unloading line gives the elastic modulus of the materials, and the enclosed area gives the elastic strain energy [82]. The energy dissipated per cycle, attributed to microcracking and internal friction, is calculated as the area of the hysteresis loop enclosed between the loading and unloading paths. For a single monotonic test without unloading, the dissipation energy can be calculated as the total energy minus the elastic strain energy calculated from the secant stiffness to the peak stress. Thus, the failure mechanism and yield deformation of MTCPB samples under impact loading is an energy absorption and dissipation process [82]. When an MTCPB specimen undergoes the UCS test, an increase in stress/strain rate results in continuous input of external energy. This input energy is subsequently converted into both elastic strain energy and dissipated energy. Assuming an adiabatic condition with no thermal exchange between the specimen and the external environment throughout the process, the energy balance can be expressed according to the first law of thermodynamics as follows [74]:

$$U = U_e + U_d \tag{2}$$

In the above equation, $U$represents the total strain energy created due to the applied external load on the MTCPB specimen in M.Jm$^{-3}$.$U_e$ denotes elastic strain energy emitted by the MTCPB specimen in M.Jm$^3$, and $U_d$ represents the energy dissipated by MTCPB, which is used by the specimen during interior damage, micro-cracking, and deformation of the specimen due to fast strain, and is also in M.Jm$^{-3}$.

During UCS experimentation only uniaxial compression is used, so the total strain energy of MTCPB can be calculated from the following equations [74,82,83]:

$$U = \int_0^{\varepsilon} \sigma \, d\varepsilon \tag{3}$$

$$U_e = \frac{1}{2E_0}\sigma^2 \tag{4}$$

$$U_d = U - U_e \tag{5}$$

Here $\sigma$ is the UCS in MPa, $\varepsilon$ is the uniaxial strain of MTCPB, and $E_0$ is the initial elastic modulus of MTCPB in the elastic region.

The curves showing the evolution of the strain energy of various MTCPB specimens under different $CO_2$ injection durations are shown in Fig. 13. Specimens under compression stage showed that the total energy, dissipated energy, and elastic strain energy increased gradually with increasing strain for different injection times. With an increase in strain, the grown in elastic strain energy is higher than the dissipated strain energy. Rapid strain growth consumes dissipated strain energy during interior damage, micro-cracking, and deformation of the specimen. In the elastic region, the energy supplied by the press is transformed and stored as elastic strain energy, while the dissipated strain energy remains nearly constant or slightly increases. During the plastic deformation stage, most of the input energy supplied by the press is still stored as elastic strain energy. However, due to the formation of new cracks and meso-pores in the specimen, the dissipated strain energy rises sharply. When the specimen reaches the peak strength stage, its capacity to store elastic strain energy reaches its limit, causing a dramatic increase in dissipated energy. At this stage, macro-cracks have been created within the samples. While the fundamental mechanism of strain energy storage, failure modes, damage pattern, and energy transformation is consistent across the entire MTCPB specimen under different $CO_2$ injection durations, the specific injection time causes significant variation in the strain energy values at peak stress.

Fig. 13 further depicts the energy distribution curves for all MTCPB specimens under different $CO_2$ injection durations. The total energy (U) and elastic energy (Ue) reveal a distinct non-monotonic trend with increasing $CO_2$ injection duration. This trend is directly corresponding to the observed strength development. Total energy (U) shows a slow increase, fast increase, and then slow decrease trend, while elastic energy displays a distinct “peak-and-declination” profile, initially rising before progressively diminishing. The corresponding rate curves for U and Ue follow an “accelerating-decelerating” sequence, whereas the dissipation energy exhibits sustained growth with progressively increasing accumulation rates. These are characteristics within the carbonated tailings composites under progressive loading.

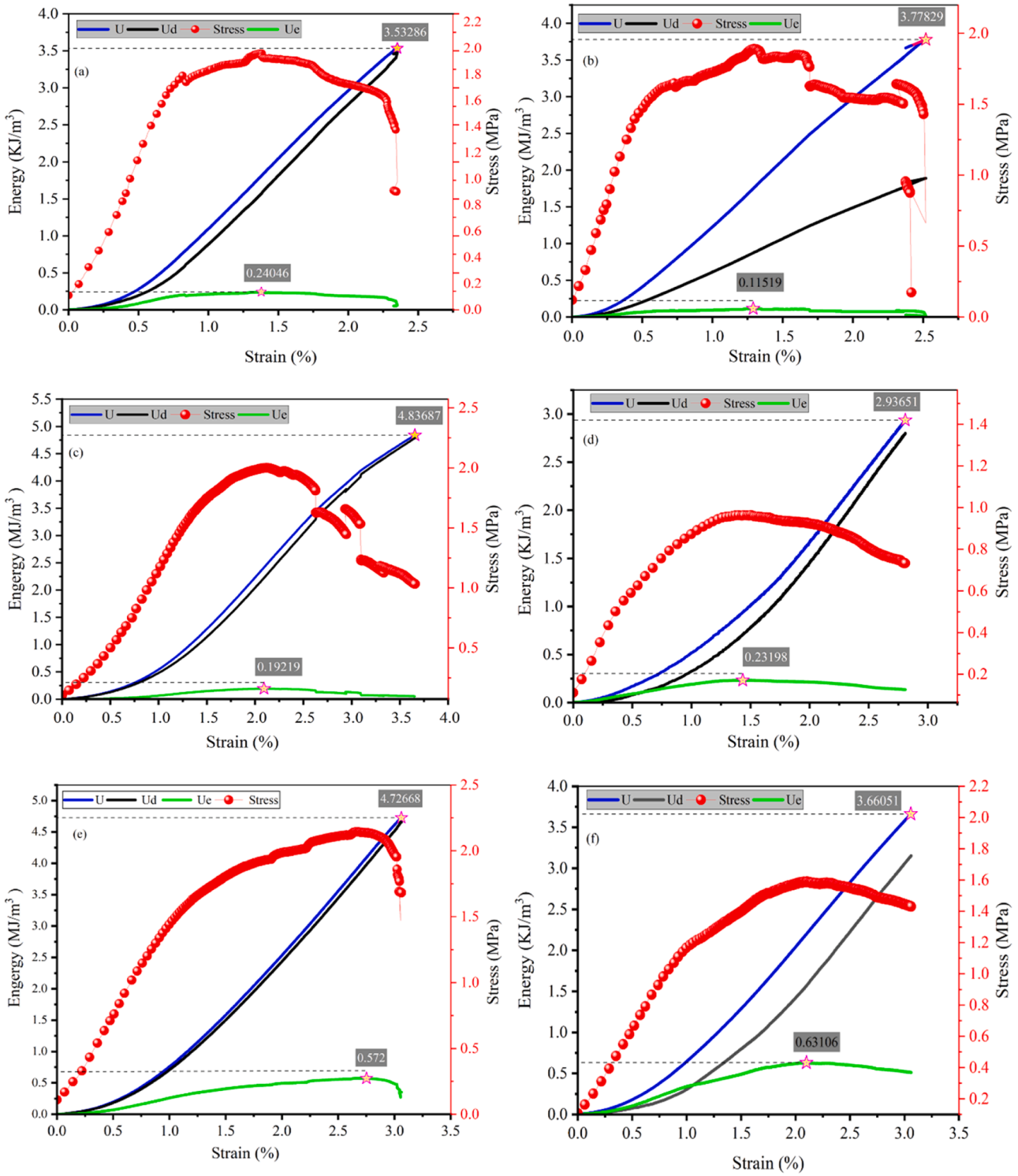



**Fig. 13.** Energy dissipation curves under compressive loading for MTCPB specimens with $CO_2$ injection durations.

The control specimen (MTCPB-0-1:6) (Fig. 13**a**) demonstrated a total energy (U) of 3.53 MJ/m$^3$ with minimal elastic strain energy (Ue) of 0.24 MJ/m$^3$ and dissipation energy (Ud) of 0.24 MJ/m$^3$. The ratio between Ud and Ue is 14.5. This high ratio indicates the characteristics of brittle failure, hydration-dominated failure, where weak interfacial bonding prevails. In this case, 98% of the input energy was irreversibly consumed by micro-crack formation [74]. During the early carbonation stages (0.5-2 minutes), the energy characteristics improved progressively with 1-minute injection and yielded 4.84 MJ/m$^3$ U, Ue, and Ud of 0.19 MJ/m$^3$ and 4.7 MJ/m$^3$, respectively. The resulting 37.1% increase in total energy relative to control demonstrates initial microstructural improvements due to $CaCO_3$ formation after carbonation, as shown in the SEM-EDS section. Similarly, after 5 and 8 minutes of $CO_2$ injection, the samples MTCPB-5 and MTCPB-8 have a total energy of 3.66 MJ/m$^3$ and 4.68 MJ/m$^3$ with their corresponding Ud and Ue as 3.15 MJ/m$^3$ 0.6 and MJ/m$^3$, 3.48 MJ/m$^3$ and 1.16 MJ/m$^3$. Under the

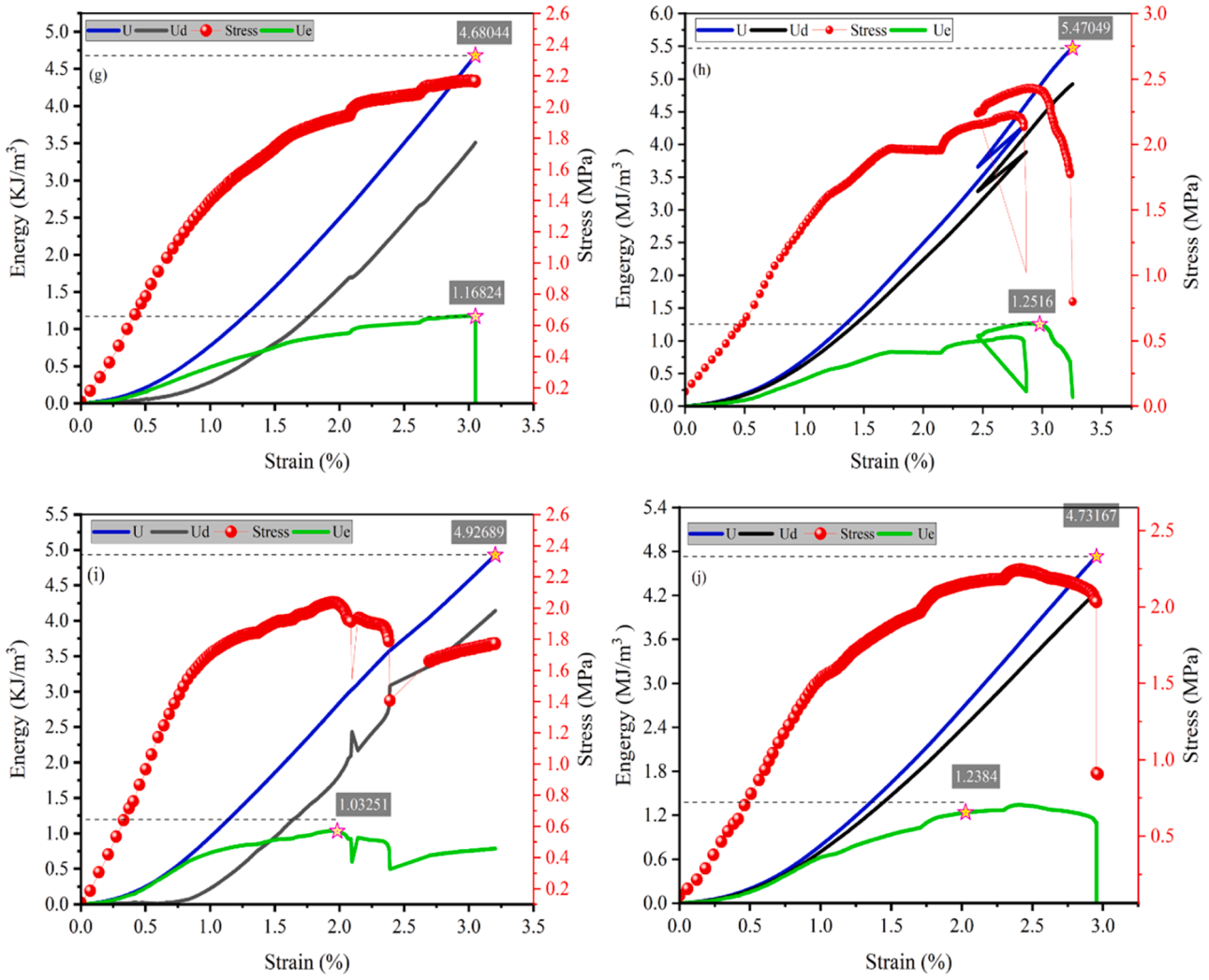



**Fig. 13.** (*continued*).

conditions investigated, the optimal carbonation groups (10 minutes) achieved peak energy performance after 10 minutes of injection, attaining a maximum total energy absorption of 5.47 MJ/m$^3$, a Ue of 1.26 MJ/m$^3$ and Ud of 4.90 MJ/m$^3$, respectively. This range indicates the carbonation efficiency threshold and illustrates an ideal balance between strength development and damage tolerance. They also suggest improved microstructure integrity through effective $CaCO_3$ bonding between tailings particles and cement hydration products.

Energy performance was substantially deteriorated beyond optimum conditions. A strength decline to 2.03 MPa was observed for MTCPB-15 with U measured at 4.92 MJ/m$^3$ and corresponding Ud and Ue values of 4.12 MJ/m$^3$ and 1.03 MJ/m$^3$, respectively.

It is seen that the total energy dissipated was only 4.73 MJ/m$^3$ for 20 minutes injection sample with associated Ue and Ud energies of 1.23 MJ/m$^3$ and 4.22 MJ/m$^3$ respectively. This represents an energy dissipation level of 13.5% reduction from peak efficiency. It is also attributed to deterioration in microstructure homogeneity due to excessive carbonation effect, leading to the presence of $CaCO_3$ statures leading to localized stress concentrations and compromising composite integrity. The evolution of failure mechanisms with increasing $CO_2$ injection duration observed in this study suggests the need for a carefully optimized balance between carbonation intensity and microstructural integrity, with the specific optimal point being dependent on the system composition and conditions investigated. The energy dissipation trend for samples with excess carbonation effect (MTCPB-15-1:6 and MTCPB-20-1:6) corroborates the carbonation saturation effect reported by Ashraf et al. [84]

### 3.6. Chemical bond characterization using FTIR

The use of FTIR spectroscopy was to determine changes occurring as a result of $CO_2$ injection into the slurry of MTCPB in the closed multi-functional chamber. Fig. 14 shows the FTIR spectra of three representative samples: MTCPB-0-1:6 (control, un-carbonated), MTCPB-10-1:6 (optimal carbonation condition), and MTCPB-20-1:6 (prolonged $CO_2$ injection) after 14 days of the curing period. The spectra revealed several characteristic absorption bands that provide detailed insights into the carbonation mechanism and mineral phase evolution of the MTCPB system.

The near-IR broad absorption band noticed in 3000-3500 cm$^{-1}$ as well as 1721 cm$^{-1}$ regions corresponds to the O-H groups stretching vibration in water molecules of hydrated products. The appearance of this broad stretching band is associated with the formation of hydrogen bonds having wide range of strengths [85]. The intensity of carbonated specimen (MTCPB-10-1:6 and MTCPB-20-1:6) is higher as compare to the non-carbonated specimens (MTCPB-0-1:6) in these regions, which indicates the presence of more hydrated products after carbonation. Therefore, $CO_2$ injection facilitates the formation of hydration products. Furthermore, there are no substantial changes in the peaks characterizing O-H bonds after 14 days of curing, showing the lack of

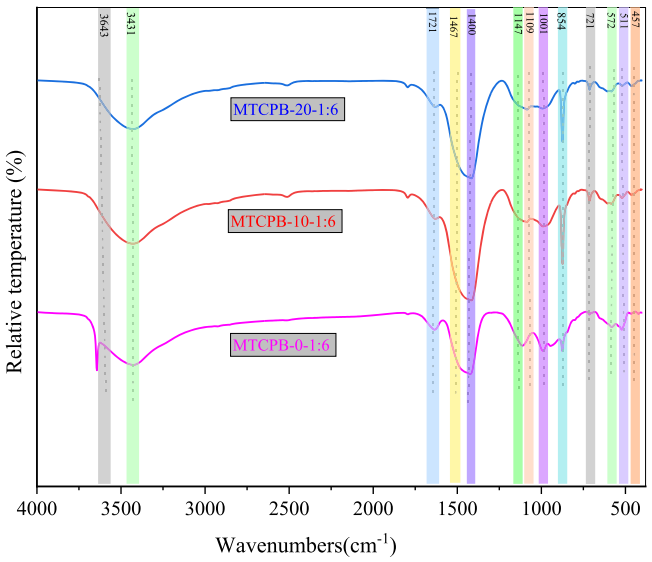



**Fig. 14.** FTIR analysis of MTCPB samples after 14 days of curing.

development of hydration products. A distinct shoulder at approximately 3643 $cm^{-1}$ was observed in the MTCPB-0-1:6 sample, which can be attributed to the vibrational band of water molecules in $Ca(OH)_2$ (Portlandite). The progressive disappearance of this shoulder at 3643 $cm^{-1}$ in MTCPB-10-1:6 and MTCPB-20-1:6 confirms the consumption of $Ca(OH)_2$ during $CO_2$ injection process, serving as the primary source of carbonate formation. This consumption was more prominent in MTCPB-10-1:6, suggesting that optimal injections are helpful in carbonated formations, while excessive $CO_2$ injections are not so in favor [86].

The mid-IR absorption band in the 1400-1467 $cm^{-1}$ region represents C-O bonds asymmetric stretching vibration in carbonate groups, while the peaks appearing at 854 $cm^{-1}$ and 721 $cm^{-1}$ correspond to out-of-plane and in-plane bending of $CO_3^{2-}$. These characteristic carbonate peak bands are minimum in the control group MTCPB-0-1:6 but show significant intensity in MTCPB-20-1:6, with further enhancement observed in MTCPB-10-1:6. The systemic increase in intensity of these carbonate bands from control to mineralized samples provides direct evidence for the formation and accumulation of calcium carbonate phases during $CO_2$ injection.

The far-IR absorption bands in the 900-1200 $cm^{-1}$ region are Si-O bonds typical asymmetric stretching vibration with absorption reached at approximately 1001 $cm^{-1}$ and 572 $cm^{-1}$ being characteristic of bending vibrations and asymmetric stretching of Si-O-Si bonds in calcium silicate hydrate (C-S-H) gel [67]. The broad bands near 511 $cm^{-1}$ are attributed to the out-of-plane skeletal vibration of Si-O bonds. The comparative analysis of three MTCPB samples showed that the characteristic bands decreased in this order: MTCPB-0-1:6 (control), MTCPB-20-1:6 (prolonged injection), and MTCPB-10-1:6 (optimal). This pattern indicates that C-S-H gel experienced decalcification and carbonation during the $CO_2$ injections. This behavior suggests that the C-S-H gel went through a decalcification process accompanied by carbonation due to $CO_2$ injection. This entails Ca removal from C-S-H gel to create $CaCO_3$.

The absorption peak of $SO4^{2-}$ group ions was seen in the range of 1109 $cm^{-1}$ to 1147 $cm^{-1}$ in all three specimens. In the case of the control specimen (MTCPB-0-1:6), the peak appeared at about 1103 $cm^{-1}$, indicating that the mineral is ettringite ($3CaO{\cdot}Al2O_3{\cdot}3CaSO_4{\cdot}32H_2O$). However, for the specimens with injected $CO_2$ (MTCPB-10-1:6 and MTCPB-20-1:6), the peak shifted to 1150 $cm^{-1}$ suggesting the transformation of ettringite into gypsum ($CaSO_4.2H_2O$).

### 3.7. TGA assessment

Thermogravimetric analysis (TGA) is an important technique to detect hydrates and carbonation compounds generated as a result of the hydration and carbonation processes of hydrated and mineralized cement-based composites [51]. By monitoring mass loss as a function of temperature at a defined heating rate, TGA enables the identification and quantification of distinct phase decomposition events [66].

Fig. 15 shows the TGA and DTG curves for three MTCPB specimens, the control (B-0), optimally carbonated (MTCPB-10-1:6), and over-carbonated (MTCPB-20-1:6) specimens after 14 days of curing. The mass loss recorded during TGA is interpreted based on the well-established literature related to the decomposition temperature of cementitious phases. For instance, phases such as gypsum, AFt, and C-S-H generally decompose between 105-200°C [66]. Portlandite dehydroxylation occurs with a corresponding increased mass loss between 390°C and 500°C, with its characteristic peak position sensitive to crystallinity and carbonation degree [35]. $CaCO_3$ de-carbonation occurs normally between 600-800°C, and poorly crystalline and amorphous carbonate phases may decomposes across a broader range of 500-800°C [53].

Fig. 15 also displays three characteristic mass loss regions in the thermograms of specimens. The first two regions that show a relatively small mass loss below 200°C. According to the literature, these thermal events correspond to the dehydration processes, including the loss of crystalline water from C-S-H and Aft [87,35]. The baseline mineralogy is established by the non-carbonated MTCPB-0-1:6 (Fig. 15**a**). The control group also exhibited a small mass change at this low temperature compared to other carbonated specimens, which may indicate a higher initial content of these hydrated phases [88]. Its TGA profile is characteristic of a hydrated cement system, dominated by a sharp, high-amplitude peak at 452°C. This corresponds to the dehydroxylation of Portlandite ($Ca(OH)_2$), accounting for a mass loss of 2.45%. A secondary well-defined peak at 698°C represents the decarbonization of calcium carbonate ($CaCO_3$), with a mass loss of 4.64%. This calcite is not a product of engineered carbonation but originates from inherent minerals in the specimen and minor natural atmospheric carbonation [66, 52], as accounted for in the control correction of Eq. (1).

Controlled $CO_2$ injection for 10 minutes induces substantial and mechanistically significant transformations in the thermogram profile of MTCPB-10-1:6 (Fig. 15**b**). The TGA curve becomes quite complicated and exhibits four mass loss events, consistent with an effective carbonation mechanism operating through multiple decomposition pathways. The first event below 200°C registers a mass loss of 2.229%, slightly reduced relative to control, consistent with the partial conversion of C-S-H during the carbonation process. The Portlandite dehydroxylation peak now shifted to 411°C with a mass loss of 1.18%. This is markedly diminished relative to the control (2.45%), confirming that a significant proportion of Portlandite was consumed as a reactant during accelerated carbonation. The downward shift of the Portlandite peak from 452°C (control) to 411°C is consistent with a reduction in the crystallite size and crystallinity of the residual Portlandite, as reported in carbonated cementitious systems [35].

Most significantly, the carbonate decomposition region evolves into two well-resolved peaks: a primary peak at 628°C (mass loss: 4.652%) and a secondary peak at 746°C (mass loss: 0.662%), yielding a total carbonate associated mass loss of 5.314%. This bimodal DTG distribution is unanimously consistent with the co-existence of thermally distinct carbonate polymorphs. The lower temperature peak (~628°C) is characteristic of metastable calcium carbonate phases, specifically vaterite or amorphous calcium carbonate and partially carbonated C-S-H, while the higher temperature peak (~746°C) reflects well-crystallized calcite [66,87]. The total $CO_2$ uptake for MTCPB-10-1:6, calculated using Equation-1, is 6.32%, which is an 84.26% increase relative to the control (3.43%). This represents the highest value recorded across all injection durations investigated and confirms that

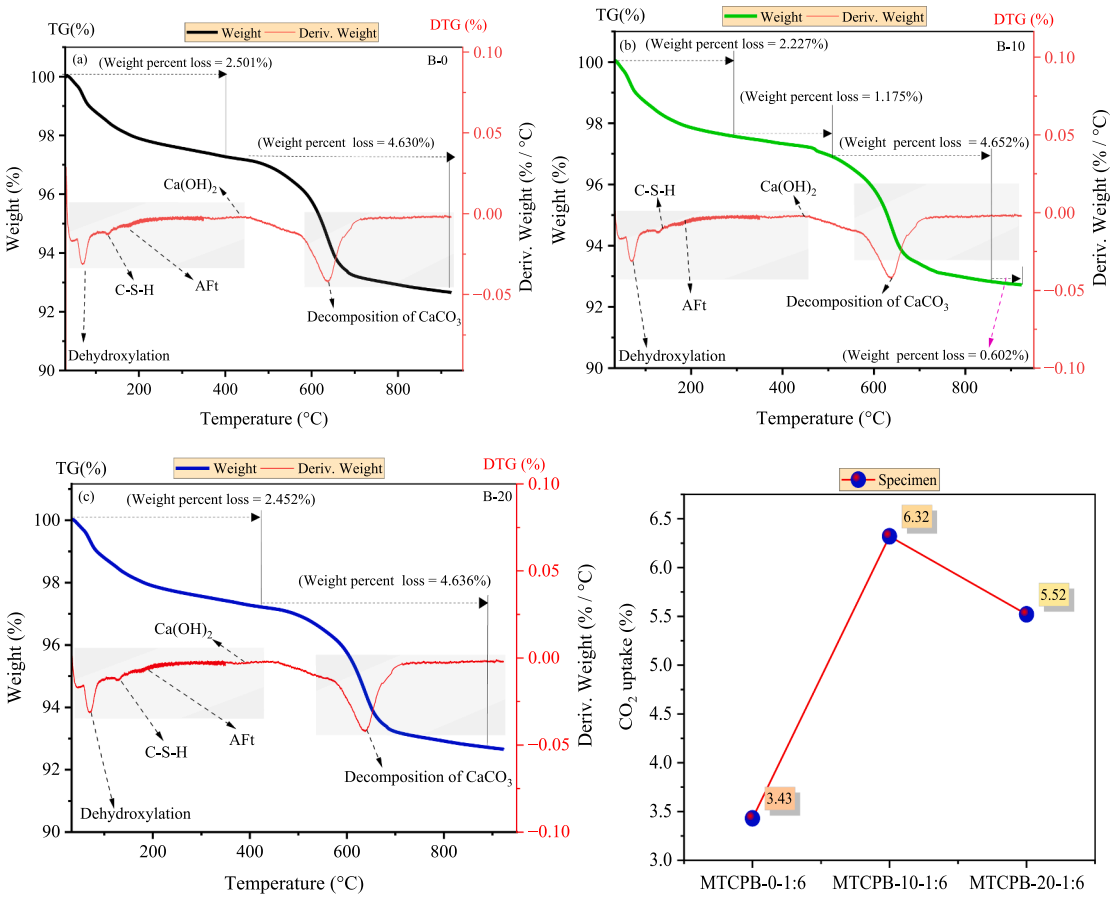



**Fig. 15.** theromograms and $CO_2$ uptake of MTCPB samples.

the 10-minute injection duration maximizes carbon sequestration efficiency under the specific conditions of this study. This state reflects a synergistic microstructural condition in which residual Portlandite and C-S-H are reinforced by nanocrystalline carbonate precipitates filling the pore network (Fig. 6 and Table 6). These thermogravimetric findings are consistent with the microstructural densification and pore refinement observed in the SEM-EDS analysis (Section 3.8) and the $Ca(OH)_2$ depletion confirmed by FTIR (Section 3.6).

Prolonged $CO_2$ injection (20 minutes) resulted in a measurable but reduced $CO_2$ uptake of 5.52%, a decline of 12.66% relative to the optimal conditions (6.32%), and represents a 51.22% increase over the control (Fig. 15**c**). The thermogram of MTCPB-20-1:6 shows a mass loss of 2.452% below 200°C and a carbonate decomposition loss of 4.696%. Notably, the Portlandite dihydroxylation peak is markedly diminished or near-absent, consistent with the near-complete consumption of available $Ca(OH)_2$ under prolonged $CO_2$ exposure. This reduction in total $CO_2$ despite prolonged injection duration is consistent with progressively pore blockage by excessive $CaCO_3$ precipitation, which stops $CO_2$ diffusion into the specimen interior. Furthermore, the near-complete depletion of reactive Portlandite combined with the absence of net carbonate gain relative to the control (4.696% vs. 4.64%) is consistent with a self-limiting carbonation behavior under over-carbonation conditions, wherein reactant exhaustion and pore blockage jointly constrain further $CO_2$ fixation. Fig. 15**d** summarizes $CO_2$ uptake across the three representative conditions: 3.43% (control), 6.32% (optimal, 10 min), and 5.52% (over-carbonated, 20 min). The TGA data make three specific contributions: (1) quantitative Portlandite consumption (from 2.45% to 1.18%), confirming $Ca(OH)_2$ as the primary carbonation reactant; (2) bimodal DTG decomposition identifying co-existing metastable vaterite (~628°C) and crystalline calcite (~746°C) polymorphs; and (3) $CO_2$ uptake quantification via Equation (1), establishing that the kinetic carbonation window is centered at 10 minutes under the specific conditions investigated. These findings are consistent with and complementary to the mechanical performance (Sections 3.1–3.5), FTIR bond analysis (Section 3.6), and SEM-EDS stoichiometric evolution (Section 3.8).

### 3.8. *Microstructural and stoichiometric evolution via SEM-EDS*

The injection of $CO_2$ through the slurry during wet carbonation promotes a dual pathway of hydration and carbonation reactions. To understand the macroscopic mechanism responsible for the macroscopic properties of MTCPB, a detailed microstructural and chemical analysis was conducted using scanning electron microscopy coupled with energy dispersive x-ray spectroscopy (SEM-EDS). These advanced characterization techniques serve in bridging the macroscopic properties with the nanoscale chemical transformations [89], enabling the visualization of micro-structural evolution, mapping of elemental distribution, and the identification of newly formed carbonation and hydration products (carbonates, silicates, ettringite etc.) [90].

#### 3.8.1. *Methodology and quantitative protocols*

In this study, ten samples with varying $CO_2$ injection durations (0-20 min) from the sealed container after 14 days of curing with a cement-to-tailings ratio of 1:6 were selected for SEM-EDS analysis. Samples were classified into five functional groups: group 1 (control, 0 min), group 2 (early carbonation, 0.5 min), group 3 (optimal/peak performance, 8-10 min), and group 4 (over carbonation/protective layer formation/passivation, 15-20 min).

Samples were coated with a thin layer of carbon to prevent the charging effect. To eliminate interference, the carbon coating was excluded from the final quantitative calculations. All elemental

compositions were normalized to 100% (Table 8) on a carbon-free basis [50]. Phase identification and extent of carbonation/mineralization were determined using specific atomic ratios (Ca/Si, Ca/(Si + Al), Al/Si, (Ca + Mg)/Si, and Al/Si) (Table 7), which are independent of the carbon coating [47]. The ratios Ca/Si and Ca/(Si +Al) were used as primary decalcification indices to track the conversion of C-S-H and C-A-S-H phases into calcium carbonate; (Ca + Mg)/Si quantified the total divalent-cation mineralization. Furthermore, Mg/Ca verified Mg-phase participation from the gold mine tailings during reactions (tailing participation), while the Al/Si ratio was used to monitor framework evolution.

The multi-elemental EDS spatial distribution maps for all four carbonation groups are provided in the supplementary material (**Figures S1–S4**), as the spatial elemental distributions they display are fully captured quantitatively in the stoichiometric ratio tables and point spectra figures presented in the main text. The 3D surface topographic metrics for all four groups are consolidated in Table 9 for direct cross-group comparison.

The stoichiometric ratios and normalized atomic percentages in Tables 10, 11, 12, and 13 are derived from n = 3–4 EDS point spectra acquired from spatially distinct locations on a single representative specimen per carbonation group. The reported standard deviations therefore reflect within-specimen spatial heterogeneity rather than inter-specimen reproducibility.

### 3.8.2. Group 1: Control/baseline hydration (0 min $CO_2$)

This sample acts as the main point of reference when studying the effects of $CO_2$-induced carbonation. This sample indicates the condition of the cemented gold mine tailings system under the normal hydraulic curing process, whereby the mechanical strength is solely derived from the conventional cement hydration process without any form of carbonation acceleration.

The SEM microstructural features (Fig. 16) reveal a heterogeneous and porous matrix as compared to the carbonated samples. The presence of distinct hexagonal plates of Portlandite ($Ca(OH)_2$) suggests a high level of free calcium hydroxide, which has not yet undergone transformation to stable carbonates. The flocculent structure, or "honeycomb," of C-S-H gel fills the interstitial spaces as the primary binding phase, and needle-like crystals of ettringite (AFt) bridge the particle gaps, providing initial tensile anchoring. The interfacial transition zone (ITZ) in this group is characterized by distinct demarcation and high localized porosity and a complete absence of secondary carbonate precipitates, acting as the composite's weak link. 3D surface reconstruction (Fig. 16 and Table 9) confirms abundant interconnected capillary pores and high surface rugosity, consistent with an unrefined pre-carbonation matrix.

The calcium concentration is measured at 7.67 at%. These data show the Ca available within the portlandite and C-S-H structures. Interestingly, the Mg content of 2 at% shows that the binder-dominated region was selected during the quantitative analysis. This indicates that even without $CO_2$ injection, the binder has successfully initiated a physical coating of tailings grains, although this coating has not yet undergone chemical mineralization. The increase in Al (9.15 at%) shows that it helped in the formation of hydration products like ettringite ($Ca_6Al_2(SO_4)(OH)_{12}.26H_2O$) and C-A-S-H. The increase in silicon (19.17 at%) confirms formation of more C-S-H gel along with primary sources (OPC) with ~20% $SiO_2$ as shown in Fig. 17.

The EDS chemical analysis confirms the chemical baseline (Table 10). The Ca/Si ratio of 0.4 is far below the actual C-S-H with a Ca/Si ratio of 1.7, indicating partial atmospheric decalcification during the 14-day curing period and the absence of accelerated carbonation. The Mg/Ca ratio of 0.261 (the highest among cement-dominated samples) confirms that Mg-bearing tailings minerals remain chemically dormant without $CO_2$ activation. The elevated Al/Si ratio of 0.477 reflects the abundant ettringite and C-A-S-H formation, while the low (Ca + Mg)/Si ratio of 0.505 establishes the minimum divalent-cation mineralization potential baseline.

EDS elemental mapping (**S1**) confirms the sharp demarcation between calcium-rich binder and tailings. Ca clusters correlate with nascent Portlandite plates and diffuse areas with moderate intensity showing C-S-H gel. Si hotspots mark tailings grains; Al concentrates in ettringite zones; O map confirms a uniform background with slight variation, and Mg signals are weak and sparse, validating the absence of Mg-phase mobilization. The ITZ appears as Ca-depleted and Si-rich zones with no secondary carbonating filling, establishing a clear starting point before $CO_2$-induced mineralization.

### 3.8.3. Group 2: Early carbonation group (0.5 min $CO_2$)

Group 2 represents the inaugural stage of accelerated carbonation. After 0.5 min of $CO_2$ injection, the system undergoes a preferential reaction with high reactivity phases. SEM micrographs (Fig. 18) reveal partial dissolution of $Ca(OH)_2$ plates: the hexagonal crystal edges become rounded and irregular, which is direct evidence of $Ca(OH)_2$ consumption to form $CaCO_3$.

A fine, granular layer of nascent calcite precipitation begins to coat the flocculant gels (C-S-H gel), showing the initiation of the nascent masking effect. AFt needles remain largely intact due to sulphate stability but are now partially embedded in the carbonate matrix, and in some places, a surface carbonate coating can be observed. The ITZ shows the first signs of mineral bridging, with fine-grained carbonated precipitates beginning to occupy interparticle gaps. The 3D topography (Table 9) shows measurable shallowing of capillary valleys related to the control, confirming that bottom-up microstructural refinement has initiated.Fig. 19

EDS chemical analysis reveals a sharp oxygen increase of 69.13% (17.5% vs. control), confirming the rapid incorporation of $CO_3^{2-}$ groups. Ca decreased 28.9% (from 7.67 to 5.45 at%) as $Ca^{2+}$ ions are mobilized from the C-S-H gel network to form discrete $CaCO_3$. Al content of 7.49 at % indicates the presence of Al-bearing phases like carbonaluminaes, while the silicon (Si) content of 12.70 at% tracks the decalcification of the C-S-H gel. Critically, the Mg/Ca ratio falls by 31.8%, confirming that $CO_2$ reacts selectively with the cement phases, while Mg-rich tailings remain dormant. The Ca/Si ratio rises slightly to 0.505 because Si is relatively more diluted by the expanding carbonate oxygen signal than Ca is lost. Al/Si increases 22.2%, indicating Al temporarily enrichment within the forming carbonated matrix (Table 11).

EDS elemental mapping (**S2**) confirms the transition from sharp chemical segregation to incipient homogenization. The Ca distribution becomes more diffuse as nascent $CaCO_3$ bridges the ITZ gaps. Si signals homogenize as carbonate phases begin occupying former C-S-H

**Table 7**
Critical atomic ratios of all sample on carbon free basis (average of spectra in each group).

| Ratios | Sample 1 | Sample 2 | Sample 3 | Sample 4 | Sample 5 | Sample 6 | Sample 7 | Min | Max |
|---|---|---|---|---|---|---|---|---|---|
| Ca/Si | 0.400 | 0.505 | 1.030 | 0.696 | 1.096 | 1.139* | 0.122* | 0.122 | 1.139 |
| Ca/(Si+Al) | 0.271 | 0.331 | 0.713 | 0.395 | 0.767 | 0.769* | 0.115* | 0.115 | 0.769 |
| Al/Si | 0.477 | 0.583 | 0.424 | 0.271 | 0.452 | 0.387* | 0.204* | 0.204 | 0.583 |
| (Ca+Mg)/Si | 0.505 | 0.590 | 1.275 | 0.825 | 1.240 | 1.991* | 1.410* | 0.505 | 1.991 |
| Mg/Ca | 0.261 | 0.278 | 0.168 | 0.151 | 0.144 | 2.038* | 18.298* | 0.144 | 18.292 |

*Outlier spectra excluded (spec 23 from sample 6, spec 27 from sample 7)

**Table 8**
Normalized atomic % of sample on carbon free basis (mean values of spectra of each group).

| Elements | Sample 1 | Sample 2 | Sample 3 | Sample 4 | Sample 5 | Sample 6 | Sample 7 |
|---|---|---|---|---|---|---|---|
| O | 58.85 | 69.13 | 57.48 | 57.51 | 55.09 | 45.63 | 62.83 |
| Na | 0.31 | 1.17 | 0.27 | 0.00 | 0.00 | 0.00 | 0.00 |
| Mg | 2.00 | 0.97 | 2.23 | 1.88 | 2.11 | 11.51 | 17.15 |
| Al | 9.15 | 7.49 | 6.12 | 4.63 | 6.63 | 4.54 | 0.96 |
| Si | 19.17 | 12.70 | 15.24 | 21.81 | 14.38 | 11.74 | 10.89 |
| S | 0.47 | 0.28 | 0.31 | 0.40 | 0.90 | 0.47 | 0.00 |
| K | 1.57 | 2.06 | 3.54 | 2.12 | 2.53 | 0.00 | 0.00 |
| Ca | 7.67 | 5.45 | 11.59 | 10.61 | 15.19 | 12.70 | 6.41 |
| Ti | 0.00 | 0.00 | 0.22 | 0.20 | 0.00 | 1.12 | 0.00 |
| Cr | 0.00 | 0.00 | 0.00 | 0.00 | 0.00 | 5.87 | 0.00 |
| Fe | 0.43 | 0.68 | 2.99 | 0.84 | 2.59 | 5.80 | 1.76 |
| Mn | 0.00 | 0.00 | 0.22 | 0.00 | 0.00 | 0.00 | 0.00 |
| Mo | 0.39 | 0.08 | 0.00 | 0.00 | 0.40 | 0.62 | 0.00 |
| Total | 100 | 100 | 100 | 100 | 100 | 100 | 100 |

**Table 9**
comparative 3D surface topographic metrics across all four MTCPB groups at 14 days of curing.

| Topographic Parameters | Control 1 control | Control 2 Early carbonation | Control 3 Optimal | Control 4 Over-carbonated |
|---|---|---|---|---|
| Peak to valley amplitude | 12-18 | 10-15 | 1-3 | 8-15 |
| Mean roughness (Ra) | 3.2 | 2.7 | 0.9 | 3-5 |
| Surface area ratio | 1.8 | 1.6 | 1.03 | 1.7-2.0 |
| Valley depth (avg) | 8-12 | 6-10 | 1-6 | 8-15 |
| Microstructural Interpretation | Pore-rich hydration matrix; capillary pores partially filled by binder nodules | Surface smoothing initiated; carbonates precipitating in pores; early pore filling underway | Near-complete pore closure achieved; near-planar surface; residual microporosity only | Regression to control-level roughness or worse; open macropores persist; passivation + $CO_2$ starvation of interior |

**Table 10**
Critical stoichiometric ratios for sample 1.

| Ratios | Value | Std Dev | Significance |
|---|---|---|---|
| Ca/Si | 0.400 | 0.235 | Baseline C-S-H decalcification index, indicates partial atmosphere carbonation |
| Ca/(Si+Al) | 0.271 | 0.156 | C-A-S-H phase stoichiometry, reflects Al incorporation |
| Al/Si | 0.477 | 0.095 | Alumino-silicate framework ratio; high due to ettringite and C-A-S-H |
| (Ca+Mg)/ Si | 0.505 | 0.307 | Total divalent cation mineralization potential |
| Mg/Ca | 0.261 | 0.193 | Cement dominant system; minimum tailings in measure region |

Note: n = 3 EDS point spectra from a single representative specimen (MTCPB-0-1:6, control, 14-day curing); standard deviations reflect within-specimen spatial heterogeneity, not inter-specimen reproducibility.

domains. Mg signals remain weak and sparse, spatially validating the kinetic preference for Ca-phase carbonation. The pervasive O signal enrichment provides direct visual confirmation of $CO_3^{2-}$ network formation throughout accessible pore space.

**Table 11**
Critical stoichiometric ratios for group 2.

| Ratios | Value | Std Dev | Significance |
|---|---|---|---|
| Ca/Si | 0.505 | 0.445 | Decalcification index, reflects Si dilution vs Ca stability |
| Ca/(Si+Al) | 0.331 | 0.277 | C-A-S-H/ carbonate phase stoichiometry |
| Al/Si | 0.583 | 0.151 | Al enrichment index, indicates carboaluminate potential |
| (Ca+Mg)/ Si | 0.590 | 0.450 | Combined divalent cation mineralization efficiency |
| Mg/Ca | 0.178 | 0.194 | Preferential cement carbonation and masking effect |

Note: n = 4 EDS point spectra from a single representative specimen (MTCPB-0.5-1:6, early carbonation, 14-day curing); standard deviations reflect within-specimen spatial heterogeneity, not inter-specimen reproducibility

**Table 12**
Critical stoichiometric ratios of optimal group.

| Ratios | Value | Std Dev | Significance |
|---|---|---|---|
| Ca/Si | 1.083 | 0.280 | Systematic $CaCO_3$ infiltration of framework |
| (Ca+Mg)/ Si | 1.240 | 0.294 | Balanced mineralization without over-precipitation |
| Al/Si | 0.471 | 0.112 | Preserved cement phase contribution |
| Mg/Ca | 0.144 | 0.074 | Ideal Ca dominance (Ca exceeds Mg) |

Note: n = 4 EDS point spectra from a single representative specimen (MTCPB-10-1:6, optimal carbonation, 14-day curing); standard deviations reflect within-specimen spatial heterogeneity, not inter-specimen reproducibility.

**Table 13**
Critical stoichiometric ratios for group 4.

| Ratios | Value | Std Dev | Significance |
|---|---|---|---|
| Ca/Si | 2.347 | 3.537 | Statistically meaning less average |
| (Ca+Mg)/Si | 5.036 | 6.096 | Extreme over mineralization |
| Al/Si | 0.204 | 0.237 | Al nearly absent relative to Si |
| Ca/(Si+Al) | 1.618 | 2.375 | Highly unstable, statistically invalid |
| Mg/Ca | 12.46 | 15.136 | Mg exceeds by 12x, catastrophic reversal |

Note: n = 3 EDS point spectra from a single representative specimen (MTCPB-20-1:6, over-carbonation, 14-day curing); standard deviations reflect within-specimen spatial heterogeneity, not inter-specimen reproducibility

#### *3.8.4. Group-3: Optimal carbonation stage-peak performance (8-10 min $CO_2$)*

This group represents the peak optimal carbonation state, exhibiting the most refined microstructural and chemical characteristics. SEM micrographs at multiple magnifications (Fig. 20) reveal a consolidated, monolithic matrix where the phase boundaries between carbonates,

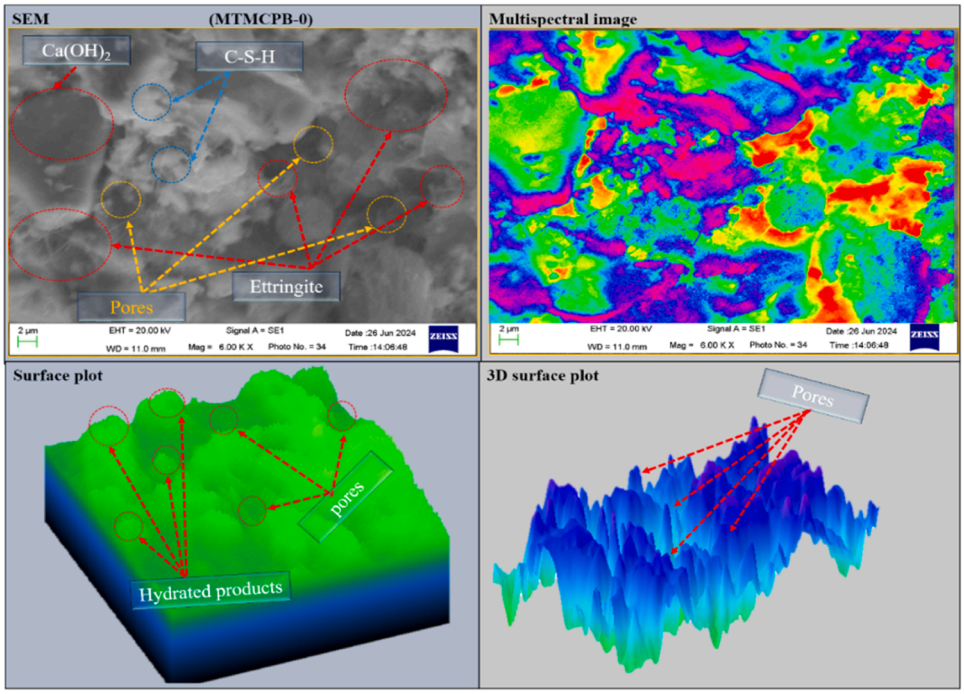



**Fig. 16.** multimodal topographic and phase analysis of control group.

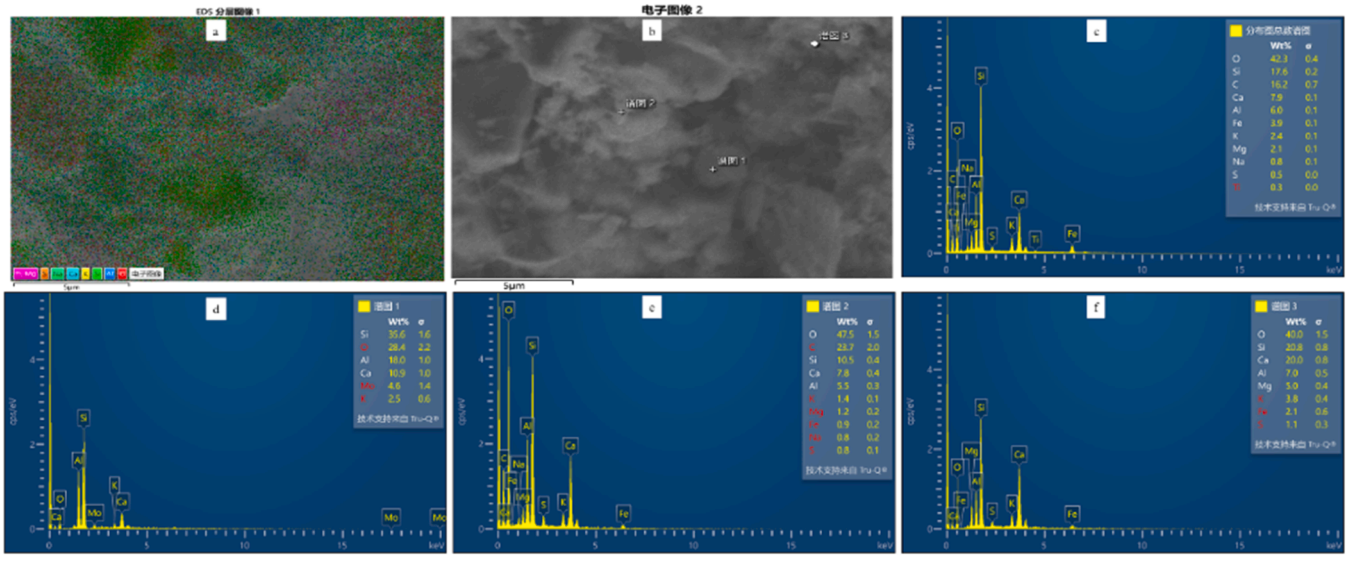



**Fig. 17.** Quantitative morphological mapping and various scanned point spectrum of control group.

silica framework, and tailings particles are essentially erased. At lower magnification (x500), striking uniformity confirms millimeter-scale $CO_2$ penetration. At a microscale (x3000-5000), thick continuous carbonate layers encapsulate all reactive surfaces: residual pores are reduced to isolated rounded voids at the practical diffusion limit; ettringite needles are buried beneath dense carbonate precipitates; and mature $CaCO_3$ phases form the primary structural bridge. Ultra-high magnification (x6000) confirms densification persists at the nanoscale: individual crystallites exhibit well-defined boundaries yet function as a unified composite. The ITZ achieves absolute obliteration. Tailing grains are so thoroughly encapsulated that they are identifiable only through elemental mapping. The 3D topographic profile (Fig. 20 and Table 9) documents the transition to a near-planar plateau with a mean roughness of 0.9 μm and a surface area ratio of 1.03. This represents the convergence point where physical and chemical optimization are simultaneously achieved.

The Mg/Ca ratio of 0.144 (Table 12) defines the optimal threshold. It indicates that for every seven moles of Ca precipitating as primary binder, only one mole of Mg is incorporated. The mineralization index ((Ca + Mg)/Si) of 1.240 represents a balanced state where carbonate precipitation fills the available porosity without excessively diluting the silicate framework. The Ca/Si ratio of 1.083 validates that carbonation has progressed to completion without triggering passivation.

EDS micro-area analysis (Fig. 21) validates the peak chemical performance. Ca content rises dramatically to 15.19 at% (+179% from the early carbonation baseline: 43.2% increase over the intermediate group). This increase reflects the complete conversion of all available Ca-bearing phases (Portlandite and all forms of C-S-H) into $CaCO_3$.

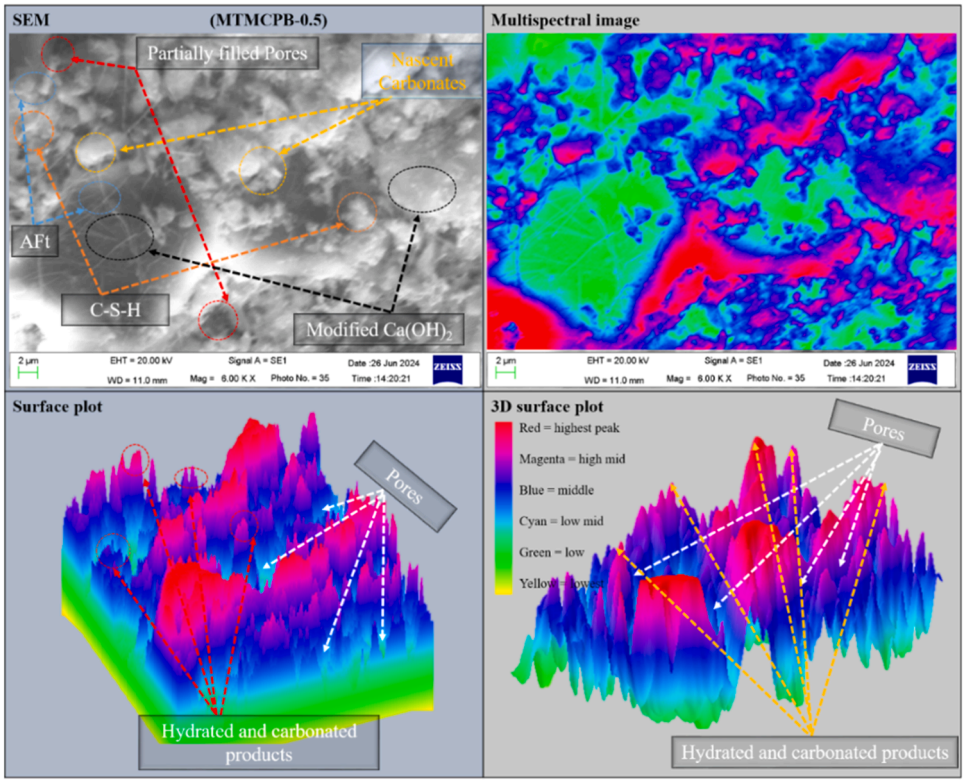



**Fig. 18.** microstructural analysis of early carbonation stage; SEM micrographs 3D surface topography.

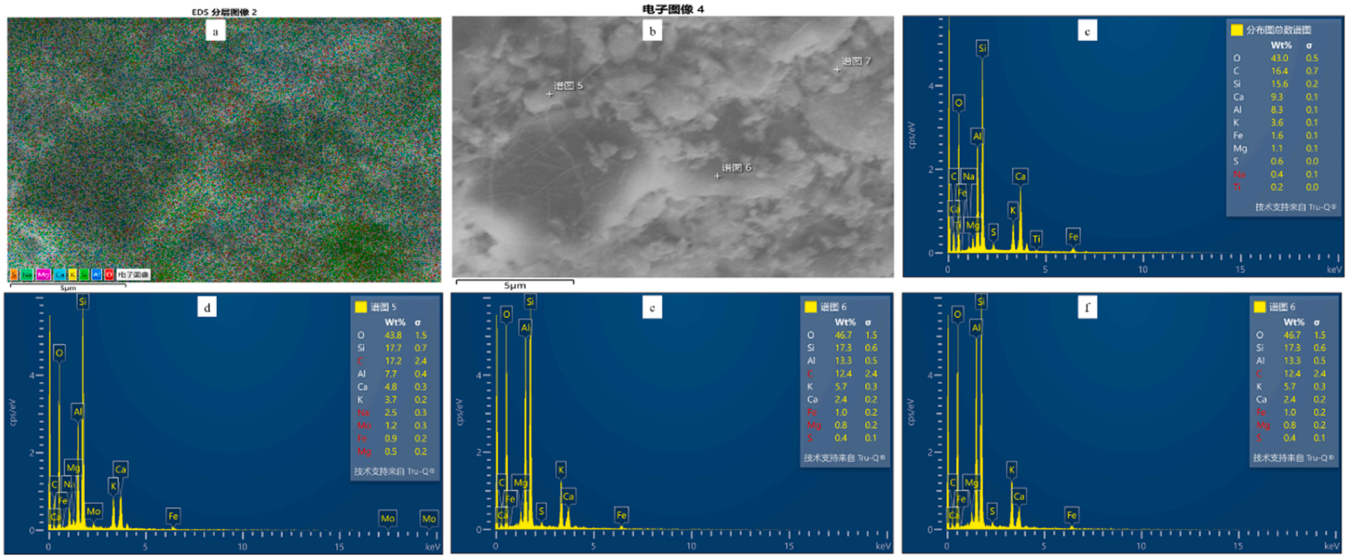



**Fig. 19.** Quantitative morphological mapping and various scanned point spectrum of group 2.

Relative heterogeneity drops 67%, falling from 7.45 at% to 3.54 at%, confirming continuous interconnected Ca-rich networks rather than isolated hotspots. Si stabilizes at 14.38 at% as the decalcified silica-gel scaffold is thoroughly infiltrated by carbonates, leading to the lowest Si heterogeneity (15% of the mean) observed across all samples. Mg stabilizes at 2.11 at% with 77% heterogeneity reduction, confirming uniform tailings-derived Mg co-participation. Al (6.61 at%) and S (0.90 at%) confirm encapsulated ettringite as stable isolated inclusions within the dominant carbonate-silicate network.

EDS elemental mapping (**S3**) provides high-resolution confirmation of peak performance. The Ca map shows a continuous, moderately intense signal forming interconnected pathways, replacing the isolated hotspots of earlier groups. Si appears as a diffuse muted background interwoven with the carbonate matrix, with no isolated bright Si zones indicating pure silica gel regions. Mg achieves widespread uniform distribution for the first time, confirming successful mobilization from tailings and co-precipitation with Ca throughout the accessible matrix. Al and Si signals are sparse and faint, confirming that ettringite is fully encapsulated. The O map shows homogenous high-intensity saturation, confirming that the system has reached carbonation equilibrium. The Fe and K maps identify inert tailings particles that are seamlessly embedded in the continuous lead-bearing composite. They serve as internal

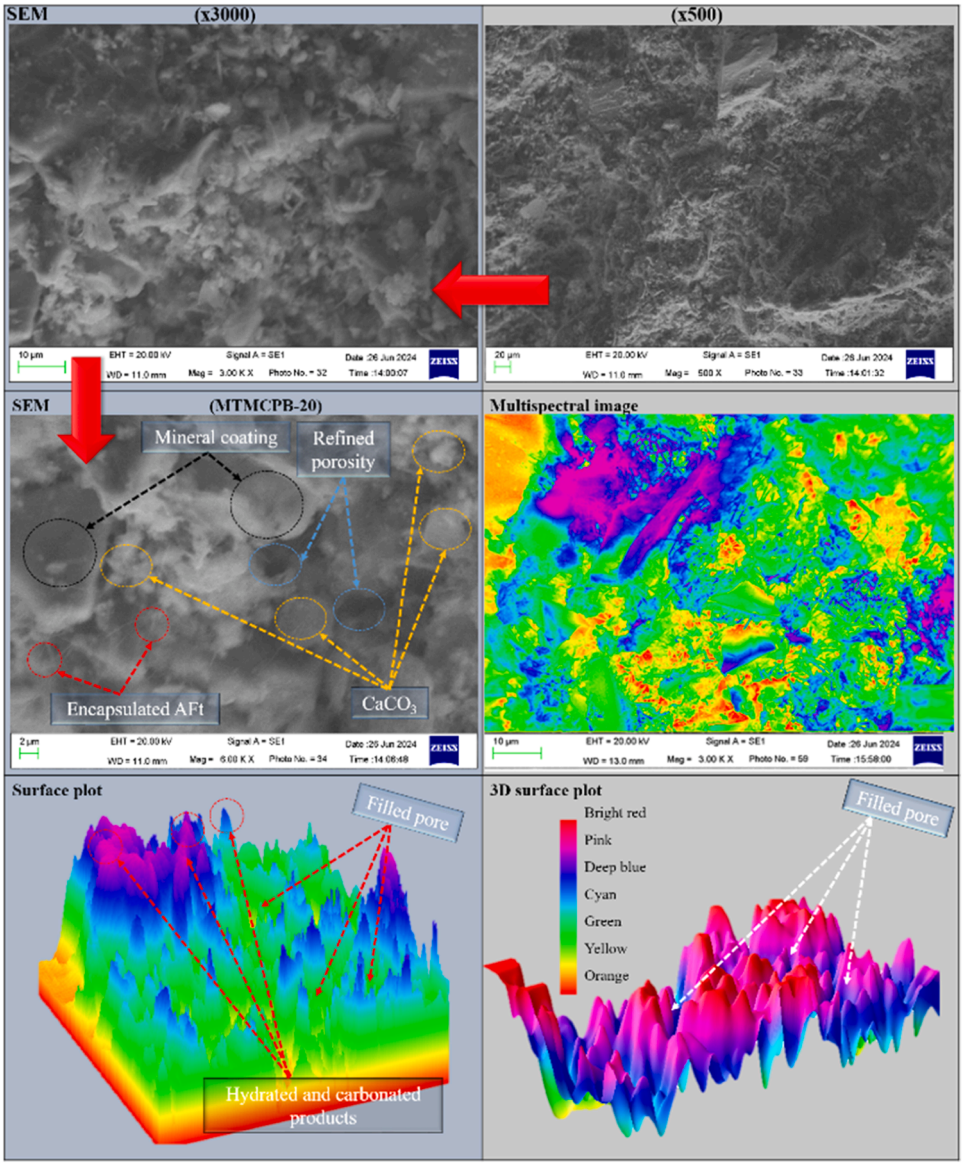



**Fig. 20.** Microstructural analysis of optimal carbonation stage; SEM micrographs (at various magnifications) and 3D surface topography.

markers confirming that ITZ is completely mineralized.

### *3.8.5. Group 4: Excessive carbonation/over-mineralization (15-20 min $CO_2$)*

Group-4 defines as an extreme anomalous regime triggered by excessive carbonation. The defining mechanism is surface passivation: initial $CaCO_3$ precipitation forms a dense impermeable surface layer that blocks further $CO_2$ diffusion into the matrix interior. The subsurface becomes $CO_2$-starved, enabling catastrophic $Mg^{2+}$ mobilization uncoupled from $Ca^{2+}$ replenishment. SEM micrograph (Fig. 22) reveals a fundamentally transformed, chaotic microstructure bearing little resemblance to cementitious composites. Distinctive passivation zones exhibit compact, low-porosity crystalline texture, forming a dual-barrier surface layer. Exposed tailings with sharp, uncoated boundaries confirm the failure of the masking effect. Density packed magnesite aggregates and platy hydomagnesite zones replace $CaCO_3$ networks of optimal samples. Dissolution-enlarged pores persist adjacent to corroded mineral edges, confirming that excessive mineralization failed to achieve complete pore closure. As a result, the interior ITZs remain permanently compromised, leaving the tailings unintegrated into the binding phase.

The 3D topographical profile (Table 9) confirms regression toward control-level roughness or worse, with a chaotic bimodal distribution: an isolated smooth plateau from surface passivation adjacent to rough, porous zones from $CO_2$ starvation. This spatial heterogeneity is the primary diagnostic marker distinguishing this group from all previous stages.

EDS analysis (Fig. 23) reveals the catastrophic endpoint of over-carbonation. Mg explodes to 17.32 at% (8.2x optimal; approaching pure mineral levels), while Ca collapses to 6.47 at% (a 57% decrease from optimal and statistically meaningless average (std = 7.81). The passivation depth gradient is directly readable in individual spectra: surface-proximal spectrum 27 (Ca = 15.89 at%, Mg/Ca ~5.5x optimal) versus deep interior spectrum 28 (Ca = 0.71 at%, Mg/Ca = 30.1, approaching pure Mg mineral composition). Al collapses to 0.97 at% (-85% vs. optimal) and S to 0.00 at%, confirming complete exhaustion of ettringite and Al-bearing cement content. The (Ca+Mg)/Si reaches 5.036 (4.1x optimal), which is above the 5.0 threshold for catastrophic over-mineralization, with individual spectra reaching 12.288 (Table 13).

The EDS elemental mapping (**S4**) provides visual confirmation of compositional chaos. The Mg map dominates with intense purple-magenta coloration across the entire scanned area, reflecting

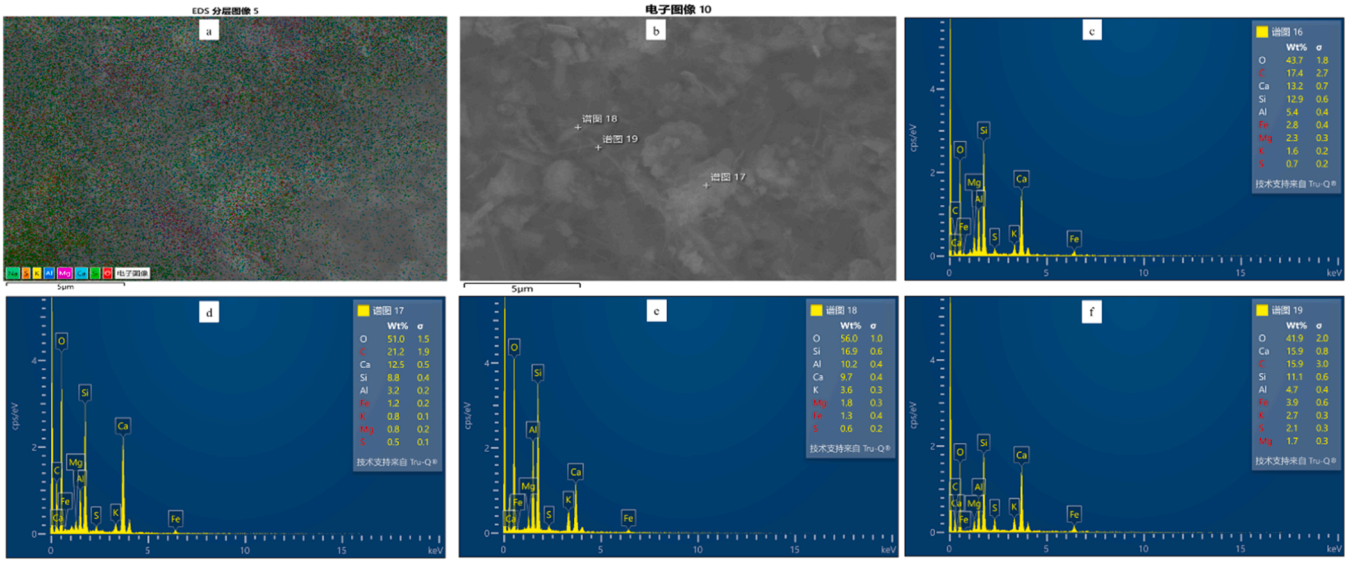



**Fig. 21.** Quantitative morphological mapping and various scanned point spectra of group 3.

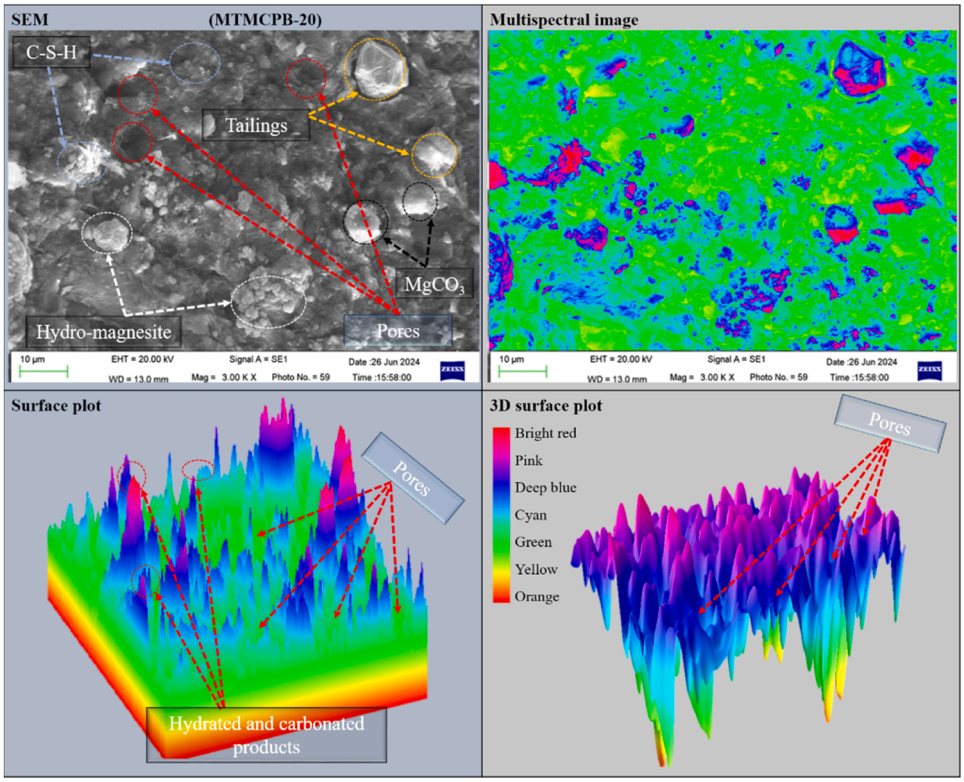



**Fig. 22.** Microstructural analysis of excessive carbonation stage; SEM micrographs and 3D surface topography.

pervasive Mg-phase formation throughout the matrix volume.

The Ca map is nearly absent, striking dark with only faint scattered spots. This validates the failure of systematic $CaCO_3$ distribution and loss of the continuous binding network. The Si map appears anomalously bright, confirming that tailing particles' surfaces remain permanently exposed and unintegrated due to passivation-arrested $CO_2$ ingress. Al appears near black throughout, validating the complete depletion of ettringite and C-A-S-H. These findings confirm that surface $CaCO_3$ passivation acted as a barrier starving the interior of $CO_2$, while simultaneously creating an incompatible phase assemblage at different depths rather than a uniform beneficial transformation.

The tailings used in this study are primarily aluminosilicate in nature ($SiO_2$: 60.13%, $Al_2O_3$: 17.82%), with relatively low CaO content (4.78%). Under standard carbonation conditions, these tailings primarily act as a physically reactive filler, providing nucleation substrates for $CaCO_3$ precipitation and mechanical reinforcement through particle–matrix interlocking. Their direct chemical participation in carbonation is limited compared with the cement phase. However, the tailings do provide $Al^{3+}$ and $Mg^{2+}$ ions that contribute to the formation of secondary phases such as C-A-S-H and Mg-bearing carbonates under prolonged $CO_2$ injection. The anomalous Mg mobilization observed at 15–20 minutes of $CO_2$ injection (Mg/Ca = 12.46 in Group 4) is

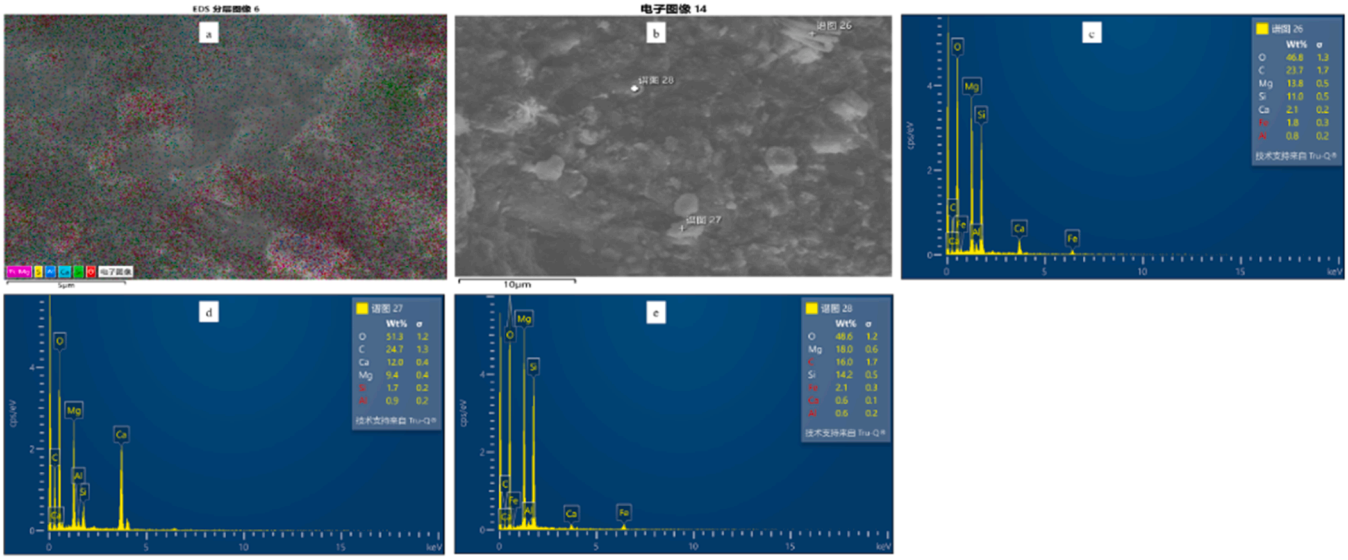


**Fig. 23.** Quantitative morphological mapping and various scanned point spectra of group-4.

attributed to $CO_2$ starvation of the cement phase due to surface passivation, which redirects the reaction toward Mg-bearing tailings minerals (likely chlorite or similar Mg-silicates) that become relatively more reactive once Ca-bearing phases are depleted.

The microstructural development of MTCPB exhibits a distinct non-monotonic pattern that aligns closely with its mechanical properties. In the control samples (MTCPB-0-1:6), the matrix displays a high surface roughness (Ra = 3.2 μm), a low Ca/Si ratio of 0.40, and a significant Portlandite content (2.45%). The presence of interconnected capillary pores results in a relatively weak, hydration-governed composite with a UCS of 2.10 MPa and an elastic modulus of 218 MPa. As $CO_2$ injection duration increases from 0.5 to 8 minutes, $CaCO_3$ precipitation within the pore structure gradually lowers Ra to 1.5–2.0 μm, shifts the Ca/Si ratio toward 1.0, and depletes the Portlandite, driving a steady rise in strength and stiffness. The system reaches its peak at the 10-minute mark (MTCPB-10-1:6), where the matrix achieves maximum refinement (Ra = 0.9 μm), a Ca/Si ratio of 1.08, and a reduction of Portlandite to 1.18%. This optimized carbonation-silicate network yields a peak UCS of 2.54 MPa, a modulus of 264 MPa, and an energy absorption capacity of 5.47 $MJ/m^3$. However, prolonged carbonation (15–20 minutes) leads to performance degradation due to surface passivation, which prevents $CO_2$ from reaching the core. This results in a sharp increase in Ra (3–5 μm), a critical rise in the Mg/Ca ratio to 12.46, and a collapse in calcium levels, causing the UCS and elastic modulus to drop to 1.30 MPa and 118 MPa, respectively. Ultimately, these results indicate that MTCPB strength is dictated by the level of microstructural densification, with 10 minutes serving as the critical kinetic threshold for balancing pore occlusion and matrix homogeneity.

### 3.9. Implications and future work

The integrated performance-based design framework developed here can be applied in the filed as sustainable mineralized CPB. Every MTCPB specimen fulfills the industry-standard UCS thresholds (0.7-1.0 MPa), confirming its technical feasibility. The net carbonated gain of 0.62% and the measured passivation boundary together establish the evidence-based guidelines for $CO_2$ injection in mine backfill. An optimal $CO_2$ injection is required to deliver adequate structural performance, controlled fracture growth, and measureable carbon sequestration. Consequently, MTCPB qualifies as a sustainable mineralized backfill material with quantifiable environmental benefits, directly aiding the mining sector's decarbonation goals by turning two major waste streams (mine tailings and $CO_2$) into structural resources. Future work should extend this framework to multi-binder systems incorporating supplementary cementitious materials (SCMs), investigate long-term carbonation stability under stress conditions and mine water exposure, and develop real-time protocols leveraging the stoichiometric markers identified here to detect and prevent passivation onset during field-scale $CO_2$ injection operations. A conceptual framework for MTCPB practical application is shown in Fig. 24. Furthermore, life-cycle accounting integrating the net carbonate gain against the energy cost of $CO_2$ injection should be quantified to establish the full environmental merit of MTCPB as a sustainable mineralized backfill at the industrial level.

### 3.10. Conclusion

This study established that $CO_2$ injection duration and curing time are precise engineering parameters capable of simultaneously tailoring the mechanical performance, failure behavior, and carbon sequestration efficiency of mineralized tailing-base cement paste backfill (MTCPB), thereby advancing the field beyond the traditional strength-only backfill design paradigm. The key scientific and practical conclusions are summarized as follows.

(1) The performance of MTCPB is governed by a critical kinetic window rather than a dose-response relationship. The non-monotonic behavior of UCS, elastic modulus, energy absorption, and microstructural integrity with respect to $CO_2$ injection

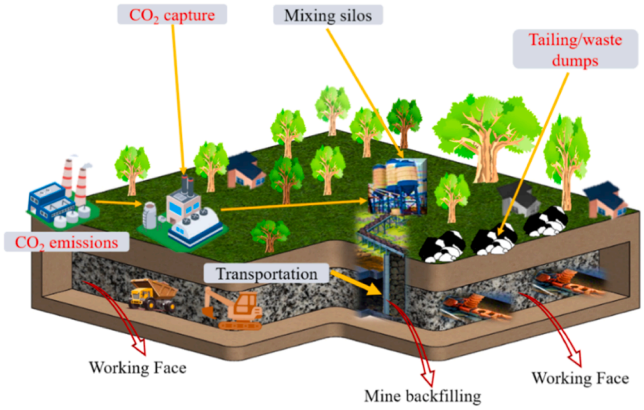



**Fig. 24.** Conceptual framework for sustainable MTCPB.

duration marks a clear departure from the commonly accepted monotonic carbonation strength link seen in conventional cementitious materials. Under the specific conditions investigated in this study, an injection duration of 10 minutes was verified as optimal, confirmed at three curing ages using quadratic and Gaussian models, simultaneously increasing UCS by 20.95%, elastic stiffness by 52% at 3 days of curing, and total energy absorption by 54.9%, while producing a net carbonate gain of 0.62%. Exceeding this window leads to surface passivation, causing a catastrophic decline in performance, a mechanistic distinction that has not yet been reported for CPB systems.

(2) Importantly, the $CO_2$ injection actively controls the failure mode of MTCPB, a structural design dimension more significant than the compressive strength alone. The transformation from brittle shear failure (control) to controlled tensile splitting (optimal, 10-min) is consistent with a carbonated-bridging crack arrest mechanism. This is verified through six-stage stress-strain analysis, which represents a qualitative shift in structural behavior with direct implications for ground support safety and prediction. This finding establishes failure modes as an explicit, controllable design output for backfill engineering, a concept unpresented in CPB carbonation literature.

(3) SEM-EDS stoichiometry defines four distinct carbonation regimes. The control group establishes baseline stoichiometry (Ca/Si = 0.400, (Ca+Mg)/Si = 0.505, Ra = 3.2 μm) characteristic of hydration-dominated matrices with dominant Mg-bearing tailings (Mg/Ca = 0.261). Optimal carbonation achieved Ca/Si = 1.083, (Ca+Mg)/Si = 1.240, and near carbonate-matrix consolidation. Over-carbonation triggered an irreversible compositional catastrophe; Mg exploded to 17.32 at%, Ca collapsed, Al depleted, and ITZ became permanently unintegrated. The Mg/Ca ratio of 12.46, representing a 12-fold excess, constitutes a quantitative stoichiometric diagnostic marker consistent with surface passivation-induced $CO_2$ starvation of the matrix interior. This is a mechanistic insight with direct implications for process monitoring in field-scale carbonation systems.

(4) The thermogravimetric investigation provided phase quantification consistent with established TGA decomposition signatures, jointly establishing the carbonation pathway, its environmental yield, and its kinetic limits. TGA-DSC identified three diagnostic mass-loss stages across all the specimens, such as dehydration of AFt and C-S-H below 200°C, $Ca(OH)_2$ decomposition at 200-500°C, and $CaCO_3$ decarbonation at 500-750°C. Under the investigated conditions, optimal $CO_2$ injection (10-min) produced substantial Portlandite consumption (1.18% vs. 2.45% in the control), accompanied by the formation of 0.62% (difference between the carbonate mass-loss fraction of the optimal specimen (5.26%) and that of the control (4.64%)) net engineered carbonate manifesting as a polymorphic mixture of metastable vaterite (~628°C) and crystalline calcite (~746°C). This mineralogical evolution underpinned the observed peak in mechanical performance. Conversely, over-carbonation (20-minute injection) resulted in no measurable net reaction (Portlandite: ~2.45%, carbonate: ~4.63%), providing thermogravimetric evidence consistent with a surface passivation layer that halted $CO_2$ diffusion, arrested the strengthening process, and reduced carbon sequestration efficiency. Therefore, the efficacy of $CO_2$ utilization in CPB is not a monotonic function of exposure time but is constrained by a precise kinetic window. To simultaneously achieve the dual objective of structural optimization and maximum carbon sequestration, the injection parameters must be precisely controlled to promote pervasive carbonation while avoiding premature pore blockage.

(5) The energy dissipation analysis reveals a toughness-based design dimension that UCS alone cannot capture. This energy framework is helpful in the CPB design methodology. Total energy absorption increased from 3.53 MJ/m$^3$ in control to 5.47 MJ/m$^3$ at optimal (+54%), where a Ud/Ue ratio of 14.5 in the control confirmed that 89% of the input energy was irreversibly consumed through uncontrolled micro-crack formation, the hallmark of brittle hydration-dominated failure. At optimal carbonation, elastic strain energy of 1.26 MJ/m$^3$ and dissipated energy is 4.73 MJ/m$^3$ reflects a damage-tolerant composite capable of controlled energy release. Over carbonation reduced total energy to 4.73 MJ/m$^3$, confirming that the energy optimum is co-located with the UCS and the microstructural optimum at 10-min injection. This progressive evolution of the Ud/Ue ratio across the full carbonation spectrum from brittle irreversible dissipation to balanced elastic storage and controlled release provides a fracture energy criterion that complements the UCS in characterizing backfill suitability for dynamic loading environments, where toughness rather than peak strength governs structural survival.

## Data availability statement

Data will be made available on request.

## CRediT authorship contribution statement

**Zahid Hussain:** Writing – original draft, Methodology, Conceptualization. **Jianxin Fu:** Supervision, Project administration, Funding acquisition, Conceptualization. **Song Weidong:** Resources, Project administration, Conceptualization. **Jiajie Li:** Methodology, Investigation, Conceptualization. **Erol Yilmaz:** Writing – review & editing, Supervision, Funding acquisition, Conceptualization.

## Declaration of competing interest

The authors declare that they have no known competing financial interests or personal relationships that could have appeared to influence the work reported in this paper.

## Acknowledgment

This research was funded by National Natural Science Foundation of China, grant number 52274109, 52474124; National Natural Science Foundation of China Youth Fund, grant number 52304120.

## Supplementary materials

Supplementary material associated with this article can be found, in the online version, at doi:10.1016/j.rineng.2026.111488.

## References

[1] M.L. Jiang, S. Cao, E. Yilmaz, Exploring microstructure and mechanical features of coupled cementitious tail-sand concrete by partial replacement of tungsten tailings, Process Saf. Environ. Prot. 190 (2024) 863–875.
[2] Z. Hussain, et al., Mapping, modeling and designing a marble quarry using integrated electric resistivity tomography and unmanned aerial vehicles: a study of adaptive decision-making, Drones 9 (4) (2025) 266, https://doi.org/10.3390/drones9040266.
[3] N.S. Yaya, S. Cao, E. Yilmaz, Innovative reinforcement: Assessing strength features of waste microplastics reinforced backfills in sustainable mine waste management, Constr. Build. Mater. 460 (2025) 139744, https://doi.org/10.1016/j.conbuildmat.2024.139744.
[4] H. Xie, Y. Wang, W. Chu, Y. Ju, Mineralization of flue gas CO2 with coproduction of valuable magnesium carbonate by means of magnesium chloride, Chin. Sci. Bull. 59 (23) (2014) 2882–2889, https://doi.org/10.1007/s11434-014-0388-1.
[5] S.O. Adewuyi, A. Anani, K. Luxbacher, Advancing sustainable and circular mining through solid-liquid recovery of mine tailings, Process. Saf. Environ. Prot. 189 (2024) 31–46, https://doi.org/10.1016/j.psep.2024.06.086.
[6] M. Koucham, Y. Ait-Khouia, S. Soulaimani, M. El-Adnani, A. Khalil, 3D geostatistical modeling and metallurgical investigation of Cu in tailings deposit: characterization and assessment of potential resources, Minerals 14 (9) (2024) 893, https://doi.org/10.3390/min14090893.

[7] N. Koukouzas, P. Koutsovitis, P. Tyrologou, C. Karkalis, A. Arvanitis, Potential for mineral carbonation of CO2 in Pleistocene basaltic rocks in Volos region (Central Greece), Minerals 9 (10) (2019) 627, https://doi.org/10.3390/min9100627.

[8] J. Li, A.D. Jacobs, M. Hitch, The effect of mineral composition on direct aqueous carbonation of ultramafic mine waste rock for CO2 sequestration, a case study of Turnagain ultramafic complex in British Columbia, Canada, Int. J. Mining, Reclam. Environ. 36 (4) (2022) 267–286.

[9] P. Allah, Exploring the use of mineral carbonation and alkali activation for the valorization of Mg-rich mine tailings, P. Allah (2022).

[10] Statista, Statista research department, Rio Tinto's Greenh. Gas Emiss. 2010-2023 (2024). https://www.statista.com/statistics/272484/rio-tintos-emissions-of-greenhouse-gases/.

[11] Z. Hussain et al., Innovative Approach to Green Mining: Integration of Drone Technology, GIS, and Ert for Basalt Extraction and CO2 Storage in Bagrote-Valley, Gilgit-Baltistan Pakistan. 2024. doi: 10.2139/ssrn.5010012.

[12] S. Kammerer, I. Borho, J. Jung, M.S. Schmidt, Review: CO2 capturing methods of the last two decades, Int. J. Environ. Sci. Technol. 20 (7) (2023) 8087–8104, https://doi.org/10.1007/s13762-022-04680-0.

[13] K. Hashimoto, K. Hashimoto, Global temperature and atmospheric carbon dioxide concentration, Glob. Carbon Dioxide Recycl. Glob. Sustain. Dev. by Renew. Energy (2019) 5–17.

[14] S.N.M. Syed Hasan, F. Mohd Kusin, N.N. Nik Daud, M.A. Saadon, F. Mohamat-Yusuff, Z.H. Ash'aari, Characterization of gold mining waste for carbon sequestration and utilization as supplementary cementitious material, Processes 9 (8) (2021) 1384, https://doi.org/10.3390/pr9081384.

[15] J. Rogelj, et al., Paris Agreement climate proposals need a boost to keep warming well below 2 °c, Nature 534 (7609) (2016) 631–639, https://doi.org/10.1038/nature18307.

[16] S. Ma, T. Lei, J. Meng, X. Liang, D. Guan, Contributions of key countries, enterprises, and refineries to greenhouse gas emissions in global oil refining, 2000–2021, Innovation 4 (1) (2023).

[17] H. Lu, C. Qi, Q. Chen, D. Gan, Z. Xue, Y. Hu, A new procedure for recycling waste tailings as cemented paste backfill to underground stopes and open pits, J. Clean. Prod. 188 (2018) 601–612, https://doi.org/10.1016/j.jclepro.2018.04.041.

[18] H. Deng, Y. Liu, W. Zhang, S. Yu, G. Tian, Study on the strength evolution characteristics of cemented tailings backfill from the perspective of porosity, Minerals 11 (1) (2021) 82.

[19] S. Cao, W. Song, E. Yilmaz, Influence of structural factors on uniaxial compressive strength of cemented tailings backfill, Constr. Build. Mater. 174 (2018) 190–201.

[20] D. Deng, Y. Gao, Z. Chen, Y. Wang, Evolutionary patterns and microscopic mechanisms of strength in mine tailings backfilled with waste glass, Sci. Rep. 14 (1) (2024) 435, https://doi.org/10.1038/s41598-023-50807-9.

[21] Y. Ghorbani, et al., Moving towards deep underground mineral resources: drivers, challenges and potential solutions, Resour. Policy 80 (2023) 103222, https://doi.org/10.1016/j.resourpol.2022.103222.

[22] C. Hou, L. Yang, L. Li, B. Yan, Mechanical characteristics and stress evolution of cemented paste backfill: effect of curing time, solid content, and binder content, Front. Mater. 8 (2022) vol. Volume-[Online]. Available: https://www.frontiersin.org/journals/materials/articles/10.3389/fmats.2021.812402.

[23] M.Z.Y.W.X. Ke, H.B. Hou, X. Zhou, Effect of particle gradation on properties of fresh and hardened cemented paste backfill, Constr. Build. Mater. 96 (2015) 378–382.

[24] G.Y.C.Y. Z, Z.H.Y.Wu H, Optimization of mix proportioning of mine filling materials using RSM-DF experiments design method, J. Basic Sci. Eng. 27 (2019) 453–461.

[25] Y.Q. Hou, S.H. Yin, Y. Cao, C.Q. Dai, Analysis of damage characteristics and energy dissipation of cemented tailings backfill with different curing ages under uniaxial compression, J. Cent. South Univ. Sci. Technol. 51 (7) (2020) 1955–1965.

[26] A. Kesimal, E. Yilmaz, B. Ercikdi, İ. Alp, H.A. Deveci, Effect of properties of tailings and binder on the short-and long-term strength and stability of cemented paste backfill, Mater. Lett. 59 (2005) 3703–3709 [Online]. Available: https://api.semanticscholar.org/CorpusID:137377345.

[27] X.Z. Zhang, D. Wu, H. Lu, L. Liu, S.L. Zheng, Improvement of tailings gradation on workability and strength of cemented tailings backfill, Constr. Build. Mater. 387 (2023) 131633.

[28] A. Assi, S. Federici, F. Bilo, A. Zacco, L.E. Depero, E. Bontempi, Increased sustainability of carbon dioxide mineral sequestration by a technology involving fly ash stabilization, Materials 12 (17) (Aug. 2019) 2714, https://doi.org/10.3390/ma12172714.

[29] W.K. O'Connor, D.C. Dahlin, D.N. Nilsen, R.P. Walters, P.C. Turner, Carbon dioxide sequestration by direct aqueous mineral carbonation, Albany Res. Center ARC, Albany, OR (2000).

[30] M.C. Dichicco, S. Laurita, M. Paternoster, G. Rizzo, R. Sinisi, G. Mongelli, Serpentinite carbonation for CO2 sequestration in the Southern Apennines: preliminary study, Energy Procedia 76 (2015) 477–486, https://doi.org/10.1016/j.egypro.2015.07.888.

[31] S. Snæbjörnsdóttir, B. Sigfússon, C. Marieni, D. Goldberg, S.R. Gislason, E. H. Oelkers, Carbon dioxide storage through mineral carbonation, Nat. Rev. Earth Environ. 1 (2) (2020) 90–102, https://doi.org/10.1038/s43017-019-0011-8.

[32] R. Ragipani, K. Sreenivasan, R.P. Anex, H. Zhai, B. Wang, Direct air capture and sequestration of CO2 by accelerated indirect aqueous mineral carbonation under ambient conditions, ACS Sustain. Chem. Eng. 10 (24) (2022) 7852–7861, https://doi.org/10.1021/acssuschemeng.1c07867.

[33] K. Lechat, J.M. Lemieux, J. Molson, G. Beaudoin, R. Hébert, Field evidence of CO2 sequestration by mineral carbonation in ultramafic milling wastes, Thetford Mines, Canada, Int. J. Greenh. Gas Control 47 (2016) 110–121, https://doi.org/10.1016/j.ijggc.2016.01.036.

[34] X. Wen, J. Fu, J. Wang, Influence of carbonation curing based on molecular sieve on the mechanical properties and microstructure of cemented tailings backfill, Constr. Build. Mater. 495 (September) (2025) 143610, https://doi.org/10.1016/j.conbuildmat.2025.143610.

[35] Y. Li, J. Fu, P. Jing, J. Wang, K. Wang, Experimental study on the macroscopic and microscopic properties of cement paste backfill after treatment with carbon dioxide carbonize filling slurries during the mixing process, J. Mater. Res. Technol. 33 (2024) 1654–1666, https://doi.org/10.1016/j.jmrt.2024.09.172.

[36] E.K. Anastasiou, M. Papachristoforou, D. Anesiadis, K. Zafeiridis, E.-C. Tsardaka, Investigation of the use of recycled concrete aggregates originating from a single ready-mix concrete plant, Appl. Sci. 8 (2018) 2149, https://doi.org/10.3390/app8112149.

[37] J. Chang, T. Jiang, K. Cui, Influence on compressive strength and CO<inf>2</inf>capture after accelerated carbonation of combination β-C<inf>2</inf>S with γ-C<inf>2</inf>S, Constr. Build. Mater. 312 (2021), https://doi.org/10.1016/j.conbuildmat.2021.125359.

[38] I. Ngo, L. Ma, J. Zhai, Y. Wang, Enhancing fly ash utilization in backfill materials treated with CO2 carbonation under ambient conditions, Int. J. Min. Sci. Technol. 33 (3) (2023) 323–337, https://doi.org/10.1016/j.ijmst.2023.02.001.

[39] Z. Hussain, J. Fu, J. Li, Y. Li, CO2 injection stirring through slurry to enhance performance of gold tailings based sustainable cement paste backfill, J. Clean. Prod. 518 (2025) 145950, https://doi.org/10.1016/j.jclepro.2025.145950.

[40] W. Sun, L. Liu, Z. Fang, G. Xie, W. He, Y. Gao, Experimental study on the production of carbon-absorbing backfill material from freshly mixed modified magnesium slag slurry, Geomech. Geophys. Geo-Energy Geo-Resour. 10 (1) (2024) 10, https://doi.org/10.1007/s40948-023-00715-z.

[41] S. Li, et al., The synergistic mechanism of hydration regulation and carbonation curing on the carbon sequestration and impermeability enhancement of cementitious materials, J. Build. Eng. 88 (2024) 109181, https://doi.org/10.1016/j.jobe.2024.109181.

[42] F.W.K. Khudhur, J.M. MacDonald, A. Macente, L. Daly, The utilization of alkaline wastes in passive carbon capture and sequestration: Promises, challenges and environmental aspects, Sci. Total Environ. 823 (2022) 153553, https://doi.org/10.1016/j.scitotenv.2022.153553.

[43] R. Zhuang, et al., Effect of moisture content on properties, microstructure and carbon sequestration of CO<inf>2</inf>-cured cement mortar mixed with chelator, J. Build. Eng. 87 (2024), https://doi.org/10.1016/j.jobe.2024.109080.

[44] A.X. Wu, Rheology of Paste in Metal Mines, Metallurgical Industry Press, 2019.

[45] B. Ke, K. Zhou, H. Deng, F. Bin, NMR pore structure and dynamic characteristics of sandstone caused by ambient freeze-thaw action, Shock Vib. 2017 (2017) 1–10, https://doi.org/10.1155/2017/9728630.

[46] C. Zhang, J. Fu, W. Song, C. Du, H. Fu, High-volume ultrafine fly ash-cement slurry mechanical properties and strength development model establishment, Constr. Build. Mater. 277 (2021) 122350, https://doi.org/10.1016/j.conbuildmat.2021.122350.

[47] K. Scrivener, R. Snellings, B. Lothenbach, and F. Group, *A practical guide to microstructural analysis of cementitious materials edited by*.

[48] T. Durdzi, M. Ben Haha, M. Zajac, and K. L. Scrivener, "Cement and concrete research phase assemblage of composite cements," vol. 99, no. May, pp. 172–182, 2017, doi: 10.1016/j.cemconres.2017.05.009.

[49] L.G. Baquerizo, T. Matschei, K.L. Scrivener, M. Saeidpour, L. Wadsö, Cement and concrete research hydration states of AFm cement phases, Cem. Concr. Res. 73 (2015) 143–157, https://doi.org/10.1016/j.cemconres.2015.02.011.

[50] J.E. Rossen, K.L. Scrivener, Materials Characterization Optimization of SEM-EDS to determine the C – A – S – H composition in matured cement paste samples, Mater. Charact. 123 (2017) 294–306, https://doi.org/10.1016/j.matchar.2016.11.041.

[51] Q. Li, J. Li, S. Zhang, X. Huang, X. Wang, and Y. Wang, "Research progress of low-carbon cementitious materials based on synergistic industrial wastes," pp. 2376, 2023, doi: https://doi.org/10.3390/en16052376.

[52] S. Hong, et al., The influence of carbon dioxide concentration on carbonation behavior in cement paste, J. Build. Eng. 88 (2024) 109104, https://doi.org/10.1016/j.jobe.2024.109104.

[53] R.I. Khan, M.I. Haque, A. Tahsin, W. Ashraf, Multiscale performance and environmental impact assessment of slag and Portland blended cement for optimum carbonation curing, CEMENT 14 (2023) 100088, https://doi.org/10.1016/j.cement.2023.100088.

[54] T. Keskin, E. Yilmaz, M. Sari, T. Kasap, Monitoring of strength and microstructure evolution characteristics of cemented paste backfill incorporating potable and non-potable water using real-time sensors, Dev. Built Environ. 24 (May) (2025) 100759, https://doi.org/10.1016/j.dibe.2025.100759.

[55] J.P.J. Aseniero, E.M. Opiso, M.H.T. Banda, C.B. Tabelin, Potential utilization of artisanal gold-mine tailings as geopolymeric source material: preliminary investigation, SN Appl. Sci. 1 (1) (2019) 35, https://doi.org/10.1007/s42452-018-0045-4.

[56] S.K. Behera, et al., Characterization of lead–zinc mill tailings, fly ash and their mixtures for paste backfilling in underground metalliferous mines, Environ. Earth Sci. 78 (14) (2019) 1–13, https://doi.org/10.1007/S12665-019-8395-9/TABLES/8.

[57] L. Yu, Y. Liu, Y. Liu, Advanced monitoring of damage behavior and 3D visualization of fiber distribution in assessing crack resistance mechanisms in steel fiber- reinforced concrete, J. Build. Eng. 97 (2024) 110980.

[58] C204 standard test methods for fineness of hydraulic cement by air-permeability apparatus (accessed, https://www.astm.org/c0204-18e01.html, Jan. 03, 2024 (accessed.

[59] T. Mashifana, T. Sithole, Clean production of sustainable backfill material from waste gold tailings and slag, J. Clean. Prod. 308 (2021) 127357, https://doi.org/10.1016/j.jclepro.2021.127357.
[60] J. Kiventerä, L. Golek, J. Yliniemi, V.M. Ferreira, J. Deja, M. Illikainen, Utilization of sulphidic tailings from gold mine as a raw material in geopolymerization, Int. J. Miner. Process. 149 (2016) 104–110, https://doi.org/10.1016/j.minpro.2016.02.012.
[61] Ö. Çelik, I.Y. Elbeyli, S. Pişkin, Utilization of gold tailings as an additive in Portland cement, Waste Manag. Res. 24 (3) (2006) 215–224, https://doi.org/10.1177/0734242X06064358.
[62] Q. Chen, Q. Zhang, A. Fourie, X. Chen, C. Qi, Experimental investigation on the strength characteristics of cement paste backfill in a similar stope model and its mechanism, Constr. Build. Mater. 154 (2017) 34–43, https://doi.org/10.1016/j.conbuildmat.2017.07.142.
[63] N. S. T. C. of L. and Resources, "DZ/T 0276.18-2015 (DZ/T0276.18-2015), Regulation for testing the physical and mechanical properties of rock.Part 18:Test for determing the uniaxial compressive strength of rock." [Online]. Available: https://www.chinesestandard.net/PDF/English.aspx/DZT0276.18-2015.
[64] X. Sun, J. Xiang, B. Xiong, X. Kong, J. Qiu, Combined biological and cement solidification of lead-zinc tailings for backfill preparation and its environmental effects, Constr. Build. Mater. 420 (2024) 135601, https://doi.org/10.1016/j.conbuildmat.2024.135601.
[65] S. Zou, S. Cao, E. Yilmaz, Effect of content of defluorinated solid waste on macroscopic strength and microstructural evolution of cemented tail filling composites, Constr. Build. Mater. 436 (2024) 136921, https://doi.org/10.1016/j.conbuildmat.2024.136921.
[66] Z. Zhang, J. Du, M. Shi, Quantitative analysis of the calcium hydroxide content of EVA-modified cement paste based on TG-DSC in a dual atmosphere, Materials 15 (7) (2022) 2660, https://doi.org/10.3390/ma15072660.
[67] X. Wang, W. Ni, J. Li, S. Zhang, K. Li, W. Hu, Use of CO2 to cure steel slag and gypsum-based material, Energies 14 (16) (2021) 5174, https://doi.org/10.3390/en14165174.
[68] S. B. Madavarapu, "FTIR analysis of alkali-activated slag and fly ash using deconvolution techniques," Arizona State University, 2014. [Online]. Available: https://www.semanticscholar.org/paper/FTIR-Analysis-of-Alkali-Activated-Slag-and-Fly-Ash-Madavarapu/ee2d450f6fefdc8b5faa9bae5869ae5bac7a5f74.
[69] Standardization administration of the People's Republic of China, "General rules for infrared analysis interpretation," no. GB/T 6040-2002. Beijing, 2002.
[70] J. Liu, S. Yao, M. Ba, Z. He, Y. Li, Effects of carbonation on micro structures of hardened cement paste, J. Wuhan Univ. Technol. Sci. Ed. 31 (1) (2016) 146–150, https://doi.org/10.1007/s11595-016-1344-5.
[71] X. He, et al., Wet grinding carbonation technique: Achieving rapid carbon mineralization of concrete slurry waste under low CO2 flow rate, Chem. Eng. J. 493 (2024) 152836, https://doi.org/10.1016/j.cej.2024.152836.
[72] N. T. Committee, "National technical committee for gold standardization (SAC/TC 379), 'technical specifications for full tailings paste backfill', GB/T 39489-2020".
[73] C. Wu, J. Li, Y. Lu, D. Zhu, The influence of industrial solid waste in conjunction with lepidolite tailings on the mechanical properties and microstructure of cemented backfill materials, Constr. Build. Mater. 419 (2024) 135422, https://doi.org/10.1016/j.conbuildmat.2024.135422.
[74] L. Liu, X. Ding, B. Tu, H. Qu, G. Xie, Energy evolution and mechanical properties of modified magnesium slag-based backfill materials at different curing temperatures, Constr. Build. Mater. 411 (2024) 134555, https://doi.org/10.1016/j.conbuildmat.2023.134555, 2024.
[75] J.X. Fu, K. Wang, J. Wang, Internal pore evolution and early hydration characterization of fly ash cement backfill, J. Build. Eng. 72 (April) (2023) 106716, https://doi.org/10.1016/j.jobe.2023.106716.
[76] Z.-X. Liu, X.-B. Li, T.-G. Dai, P. Cao, On damage model of cemented tailings backfill and its match with rock mass, Yantu Lixue/Rock Soil Mech. 27 (9) (2006) 1442–1446.
[77] S. Zhang, et al., Research on the strength influence and crack evolution law of layered backfill based on macro and meso mechanical response, Constr. Build. Mater. 449 (2024) 138493, https://doi.org/10.1016/j.conbuildmat.2024.138493.
[78] J. Wang, J. Fu, W. Song, Y. Zhang, Effect of rice husk ash (RHA) dosage on pore structural and mechanical properties of cemented paste backfill, J. Mater. Res. Technol. 17 (2022) 840–851, https://doi.org/10.1016/j.jmrt.2022.01.044.
[79] C. Zhang, J. Fu, W. Song, M. Kang, T. Li, N. Wang, Analysis on mechanical behavior and failure characteristics of layered cemented paste backfill(LCPB) under triaxial compression, Constr. Build. Mater. 324 (2022) 126631, https://doi.org/10.1016/J.CONBUILDMAT.2022.126631.
[80] E. Yilmaz, B. Koohestani, S. Cao, Recent practices in mine tailings' recycling and reuse, INC (2023), https://doi.org/10.1016/B978-0-323-91283-9.00013-4.
[81] H. Qin, S. Cao, E. Yilmaz, Mechanical, energy evolution, damage and microstructural behavior of cemented tailings-rock fill considering rock content and size effects, Constr. Build. Mater. 411 (2024) 134449, https://doi.org/10.1016/j.conbuildmat.2023.134449, 2024.
[82] J. Wang, C. Zhang, W. Song, Y. Zhang, The Energy dissipation, AE characteristics, and microcrack evolution of rock–backfill composite materials (RBCM), Minerals 12 (4) (2022) 482, https://doi.org/10.3390/min12040482.
[83] Q. He, E. Yilmaz, L. Sun, S. Cao, Influence of alkaline agents with different contents on strength features, energy dissipation and microscopic behavior of cement-based high-sulfur tailings fill, Powder Technol. 444 (May) (2024) 120042, https://doi.org/10.1016/j.powtec.2024.120042.
[84] W. Ashraf, J. Olek, Elucidating the accelerated carbonation products of calcium silicates using multi-technique approach, J. CO2 Util. 23 (2018) 61–74.
[85] S. Zhang, et al., The mechanism of hydrating and solidifying green mine fill materials using circulating fluidized bed fly ash-slag-based agent, J. Hazard. Mater. 415 (2021) 125625, https://doi.org/10.1016/j.jhazmat.2021.125625, 2021.
[86] X. Wang, W. Ni, J. Li, S. Zhang, M. Hitch, R. Pascual, Carbonation of steel slag and gypsum for building materials and associated reaction mechanisms, Cem. Concr. Res. 125 (2019) 105893, https://doi.org/10.1016/j.cemconres.2019.105893, 2019.
[87] T. Lan, et al., Manufacture of alkali-activated and geopolymer hybrid binder (AGHB) by municipal waste incineration fly ash incorporating aluminosilicate supplementary cementitious materials (ASCM), Chemosphere 303 (2022) 134978, https://doi.org/10.1016/j.chemosphere.2022.134978.
[88] P. Gong, et al., Investigation of microstructure and mechanical property evolution in a novel low-cost Ni-free maraging steel based on Mn and C through cold rolling followed by aging, J. Mater. Res. Technol. 33 (2024) 6732–6743, https://doi.org/10.1016/j.jmrt.2024.11.029.
[89] R. Masoudi, R.D. Hooton, Examining the hydration mechanism of supersulfated cements made with high and low-alumina slags, Cem. Concr. Compos. 103 (2019) 193–203 [Online]. Available: https://api.semanticscholar.org/CorpusID:164237381.
[90] X. Mu, et al., Performance optimization and hydration mechanism of a clinker-free ultra-high performance concrete with solid waste based binder and steel slag aggregate, J. Build. Eng. 63 (2023) 105479.